Int J Earth Sci (Geol Rundsch) (2015) 104:565–586
DOI 10.1007/s00531-014-1112-8

ORIGINAL PAPER

The Ordovician Las Chacritas pluton (Sierra de Humaya, NW Argentina): origin and emplacement triggered by lateral shortening and magmatic stoping at mid-crustal level

Mariano A. Larrovere · Pablo H. Alasino · Camilo R. de los Hoyos · Arne P. Willner

Received: 17 March 2014 / Accepted: 15 November 2014 / Published online: 5 December 2014

Abstract Field relationships and structural studies combined with in situ U–Th–Pb dating of monazite from Las Chacritas pluton (LCP), Sierra de Humaya, provide insight into the emplacement of peraluminous magmas triggered by lateral shortening of the host rock and magmatic stoping at a mid-crustal level of a retro-arc zone in a convergent orogen. Modal and chemical compositions indicate that the LCP is composed of two main igneous units of peraluminous granitoids. The predominant two-mica granitoids were generated by interaction of crustal rocks with mafic or mafic-derived magmas and/or crystal-rich magmas that entrained residual phases, whereas less abundant leucocratic granitoids may have been originated by partial melting of metasedimentary rocks. The calculated crystallization age of 474 ± 4 Ma is consistent with Ordovician ages (477–470 Ma) of the high-grade metamorphic rocks, indicating concomitant magmatism and metamorphism during the Famatinian orogeny. The LCP was emplaced in the middle crust at a maximum depth of ~14.5 km, where attendant fracturing and ductile deformation were active. Field evidence shows strong temporal and spatial relationships between host rock ductile deformation and the emplacement of the pluton such as folding and strike deflection of the host rock layering and folded concordant leucocratic sheets with magmatic fabrics. This suggests that material transfer processes like lateral wall rock displacement (lateral shortening) was a viable mechanism for the emplacement of the LCP. However, cross-sectional restoration and field evidence such as wall rock xenoliths and intrusive truncations of the host rock foliation and fold traces suggest that magmatic stoping was a complementary mechanism to create the necessary space for the emplacement of the LCP. This work supports previous studies showing that participation of multiple material transfer processes are the rule rather than the exception in the emplacement of plutons.

Keywords Petrogenesis · Emplacement · Ductile deformation · Stoping · U–Pb–Th dating · Las Chacritas pluton

Electronic supplementary material The online version of this article (doi:10.1007/s00531-014-1112-8) contains supplementary material, which is available to authorized users.

M. A. Larrovere (✉) · P. H. Alasino
Centro Regional de Investigaciones Científicas y Transferencia Tecnológica La Rioja, Consejo Nacional de Investigaciones Científicas y Técnicas (CRILAR-CONICET), Entre Ríos y Mendoza, 5301 Anillaco, La Rioja, Argentina
e-mail: marianlarro@gmail.com

M. A. Larrovere · P. H. Alasino
Instituto de Geología y Recursos Naturales, Centro de Investigación e Innovación Tecnológica, Universidad Nacional de La Rioja (INGeReN-CENIIT-UNLaR), Av. Gob. Vernet y Apóstol Felipe, 5300 La Rioja, Argentina

C. R. de los Hoyos
Leonidas Aguirre 67, 5500 Mendoza, Argentina

A. P. Willner
Institut für Geologie, Mineralogie und Geophysik, Ruhr-Universität, 44780 Bochum, Germany

Introduction

Magma bodies in the crust are gravitationally unstable since less-dense low-viscosity material is placed below denser higher viscosity material. This energetically unstable situation leads to magma bodies moving upward until they reach gravitational equilibrium or solidify (Hogan et al. 1998). Although magma buoyancy is the driver of pluton ascent,

stresses generated by degassing, aureole thermal gradients, and tectonic also play an important role (Hogan et al. 1998; Paterson and Farris 2008). Magma ascent and emplacement also have been associated to crustal-scale shear zones (e.g., Brown and Solar 1998a, b; Weinberg et al. 2004). In response to an upward moving magma body, the overlying crust moves upwards, downwards or laterally (Paterson and Farris 2008) involving complex physical interactions, i.e., material transfer processes (MTPs) (Buddington 1959; Paterson et al. 1996). Petrologic and structural studies of Cordilleran plutons conclude that magma emplacement in continental crustal sections typically involves multiple MTPs which may vary with distance, depth and time (e.g., Paterson and Fowler 1993; Miller et al. 2009).

In Ordovician times, widespread magmatism on the southwestern continental margin of Gondwana was coeval with a regional medium- to high-temperature (T)/low- to medium-pressure (P) metamorphism linked to eastward subduction of an oceanic plate and substantial crustal thickening. This broad magmatic arc in NW Argentina is known as the Famatinian orogen (Willner et al. 1987; Pankhurst et al. 1998, 2000; Lucassen and Franz 2005). Currently, the middle-to-upper crustal rock record of this tectono-metamorphic and magmatic event is widely exposed in the Sierras Pampeanas crystalline basement due to erosion-driven long-term exhumation until Carboniferous times and later to exposure by Cenozoic Andean tectonic faulting (e.g., Jordan and Allmendinger 1986). The extensive batholith-scale Ordovician magmatism was interpreted as the Famatinian magmatic-arc zone characterized by I-, S- and transitional I/S-type granitoids and minor mafic rocks (Pankhurst et al. 1998, 2000; Saavedra et al. 1998; Otamendi et al. 2009; Grosse et al. 2011). In the retro-arc zone to the east, minor isolated granitoid plutons that intruded into metasedimentary host rocks represent the innermost documentation of the Famatinian magmatism (Toselli et al. 1983; Llambías et al. 1998; Pankhurst et al. 2000; Dahlquist et al. 2012). A plethora of geochemical, isotopic and geochronologic studies (Knüver 1983; Reissinger 1983; Toselli et al. 1983, 1996; Rapela et al. 1990; Toselli 1992; Llambías et al. 1998; Pankhurst et al. 1998, 2000; Saavedra et al. 1998; Rossi et al. 2002; Sato et al. 2003; Cisterna 2003; Cisterna et al. 2004; Dahlquist and Galindo 2004; Büttner et al. 2005; Dahlquist et al. 2005, 2007, 2008, 2012, 2013; López de Luchi et al. 2007; Fernández et al. 2008; Morosini et al. 2009; Otamendi et al. 2009, 2012; Ducea et al. 2010; Chernicoff et al. 2010; Sola and Becchio 2010; Grosse et al. 2011; Steenken et al. 2011; Casquet et al. 2012) attempted to unravel the origin and geotectonic evolution of the Famatinian magmatism. The core works focus on the regional evolution of granitic batholiths from the main Famatinian magmatic arc (Sierras de Capillitas, Velasco, Chepes, Famatina and Valle Fértil), whereas less attention was given to the more scattered magmatism located on the dominant medium- to high-grade metasedimentary retro-arc zone (e.g., Sierras de Ambato, Ancasti, Aconquija, and Quilmes). The relationship between plutons and high-grade metamorphic terranes is potentially significant to link the generation, segregation, ascent and emplacement of the granitic magma. Vertically extensive crustal sections are excellent natural laboratories to evaluate the physical and chemical properties of magmatic bodies and processes acting to form plutons at different crustal levels (Miller et al. 2009). This has important implications because melt transfer alters the thermal and rheological behavior of the crust during orogenesis (Solar and Brown 2001; and references therein).

Here, we focus on the Las Chacritas pluton (LCP) and its host rocks in the Sierra de Humaya, Sierras Pampeanas, NW Argentina. First, to define the petrogenesis of the LCP, we report its absolute age, petrography, mineral chemistry, and bulk major and trace element composition. Second, we present detailed field and structural data to constraint the mechanisms and physical conditions of the emplacement of the LCP at a mid-crustal level of a retro-arc zone in a convergent orogen.

Geologic setting

The Famatinian belt

The Famatinian belt is an up to 200 km broad and over 1,000 km NNW–SSE trending belt mainly represented by Ordovician sedimentary-derived metamorphic and granitoid rocks, and minor volcanic rocks formed during the Famatinian orogeny (Aceñolaza and Toselli 1973) as result of a major subduction event along the Cambrian continental margin of Gondwana (Willner et al. 1987; Pankhurst et al. 1998). The Famatinian orogeny was defined in the Sierras Pampeanas and the Altiplano-Puna region in the central and northwestern region of Argentina, but an Ordovician arc extended from the La Pampa Province (ca. 39°S latitude; Chernicoff et al. 2010) via the coast of southern Peru and the Eastern Cordillera of northern Peru to Venezuela and Colombia (ca. 10°N latitude; Chew et al. 2007), suggesting that the entire western part of the Gondwana margin was active. From west to east in the eastern Sierras Pampeanas, three main geotectonic domains are found in the Famatinian belt: an accretionary wedge zone, an arc zone and a retro-arc zone (Otamendi et al. 2008; Larrovere et al. 2011). The accretionary wedge zone is located in the west side of the Sierra de Valle Fértil and consists of metamorphic rocks with strong isothermal decompression paths (Vujovich 1994; Baldo et al. 2001; Otamendi

et al. 2008; Casquet et al. 2012). The arc zone consists of calc-alkaline batholiths composed of I-, S- and transitional I/S-type granitoids with εNd_{470} values of ~−4 to −5.5, ~−4.5 to −8.5 and ~−4 to −6, respectively (Toselli et al. 1996; Pankhurst et al. 1998; Saavedra et al. 1998; Dahlquist and Galindo 2004; Grosse et al. 2011). In the westernmost region of the Famatinian arc, mafic magmatism with a wide isotopic range (εNd_{470} ~−5.5 to 4.5) has been reported as well as granulite facies migmatites (Pankhurst et al. 2000; Otamendi et al. 2008, 2009, 2010; Casquet et al. 2012). The retro-arc zone is characterized by medium- to high-grade metamorphic rocks and minor scattered plutons (Büttner et al. 2005; Larrovere et al. 2011; Steenken et al. 2011). In the Cachi and Quilmes ranges (ca. 25°–26°S latitude), the metamorphic evolution and the emplacement of plutons took place in an extensional retro-arc setting linked to the Famatinian subduction (Büttner et al. 2005; Hongn et al. 2014). The broad high-grade metamorphism and the associated coeval magmatism in the Famatinian belt are consistent with a widespread high thermal regime during Ordovician times (Lucassen and Becchio 2003; Lucassen and Franz 2005; Otamendi et al. 2008; Larrovere et al. 2011). Stacking of the magmatic arc occurred during the Ordovician and Silurian resulting in a crust with excess thickness similar to the present central Andes (Willner et al. 1987; Lucassen and Franz 2005; de los Hoyos et al. 2011).

The Sierra de Humaya

The Sierra de Humaya is an igneous–metamorphic basement block located in the northeastern region of the eastern Sierras Pampeanas, i.e., in the retro-arc zone of the Famatinian belt (Fig. 1a; for more regional details see Fig. 1 from Larrovere et al. 2011). The basement is dominated by widespread metasedimentary rock sequences and small intrusive igneous bodies (González Bonorino 1950), all grouped together as the El Portezuelo metamorphic–igneous complex (Larrovere 2009). Predominant metamorphic rocks in the Sierra de Humaya are garnet-bearing migmatite and gneiss, cordierite–garnet–K-feldspar–sillimanite migmatite, biotite–feldspar gneiss and migmatite, as well as two-mica gneiss and schist. The main metamorphic foliation (S2 regional foliation, nomenclature of Larrovere 2009) strikes NNW–SSE/N–S and dips at intermediate angles toward the east. In the northern part of the Sierra de Humaya, the prograde metamorphism increases across strike to the west, from greenschist to granulite facies in units showing structural continuity (Fig. 1b, c). The protoliths of these rocks were the Late Neoproterozoic—Early Cambrian low-grade metamorphic rocks of the Puncoviscana Formation that originally belonged to sequences of clastic sedimentary rocks mainly composed of graywacke and shale (Aceñolaza and Toselli 1973; Willner et al. 1990; Adams et al. 2011; Escayola et al. 2011; Larrovere et al. 2012). The migmatization of the El Portezuelo metamorphic–igneous complex took place during the Famatinian orogeny between 477 and 470 Ma (ID-TIMS U–Pb in monazite, three dates: 471 ± 1, 470 ± 12 and 477 ± 5 Ma, errors 2σ; Larrovere et al. 2011). The thermal peak metamorphic conditions were 670–820 °C and 4.5–5.3 kbar, consistent with a high-T/medium-P metamorphism developed at mid-crustal levels (~17–21 km depth). Scattered concordant meter- to decameter-scale igneous bodies intruded these metamorphic rocks. They consist of tonalite and granodiorite, and the LCP represents the largest magmatic body (kilometer-scale) in the Sierra de Humaya (Fig. 1b).

Analytical methods

The mineral chemical analyses were carried out at the Institut für Mineralogie und Kristallchemie, Stuttgart University, Germany, using a Cameca SX100 electron microprobe with five WDS to determine the concentrations of Na, Mg, Al, Si, K, Ca, Ti, Mn, Fe and Ba. Counting times were 20 s at the peak and on the background. For a few elements (Na, Ti and Mn) longer counting times up to 60 s and a large PET and LiF analysator crystal were used. Synthetic and natural minerals, glasses and pure oxides were used as standards. The applied acceleration voltage and electric current were 15 kV and 15 nA, respectively. The beam diameter was about 5 µm. The PAP correction procedure provided by Cameca was applied.

For in situ U–Th–Pb dating of monazite (EPMA geochronology), we used the same microprobe. The measurements were achieved on thin sections coated with a 30-nm carbon layer. Analyses were performed with a 15-kV acceleration voltage and 30-nA beam current. For each full analysis of monazite, the most common rare-earth elements (REEs) and Pb, U, Th, P, Ca, Si and Y were measured using the following emission lines and standards: Ca-Kα (diopside), U-Mß (U-bearing glass), Th-Mα (Th-bearing glass), Pb-Mß (PbTe), Ce-Lα (synthetic REE-rich glass delivered by P&H Developments, England), La-Lα (sythetic REE-rich glass), P-Kα (apatite), Y-Lα (synthetic REE-rich glass), Pr-Lß (synthetic REE-rich glass), Nd-Lα (synthetic REE-rich glass), Sm-Lα (synthetic REE-rich glass), Gd-Lß (synthetic REE-rich glass) and Si-Kα (orthoclase). Oxygen was not measured but calculated by stoichiometry. For the background measurements of REEs, we followed the recommendations of Reed and Buckley (1998). The counting times on both peak and background for the critical elements Pb, U and Th were 300 s for Pb-Mß, 150 s for U-Mß and Th-Mα, 600 s for

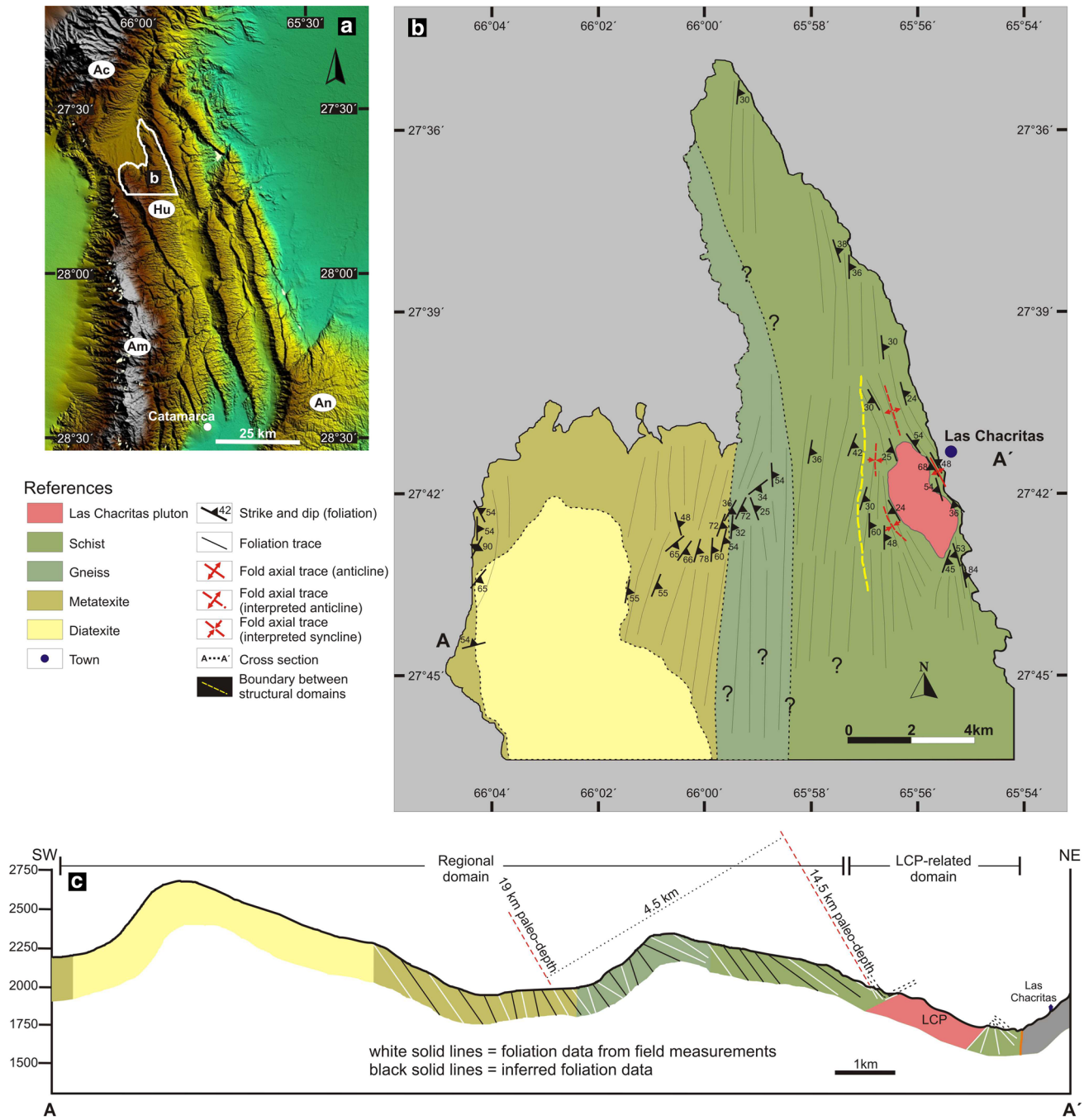

Fig. 1 **a** Location of the study area in the northeastern eastern Sierras Pampeanas. *Ac* Sierra de Aconquija, *Am* Sierra de Ambato, *An* Sierra de Ancasti, *Hu* Sierra de Humaya. **b** Geological map and **c** geological cross section of the northern part of the Sierra de Humaya. Estimated paleo-depths and structural domains are shown in the cross section

Pb-Mß, and 300 s for U-Mß and Th-Mα. We measured U and Th with a normal-sized PET spectrometer crystal, while Pb was analyzed using a large PET crystal. Similar to Scherrer et al. (2000), a (small) correction of the U-Mß peak was applied due to the contribution of the Th-Mγ line. The counting times for all other elements ranged between 200 and 20 s for both peak and background. All REEs were measured with LiF (lithium fluoride) spectrometer crystals.

The whole-rock chemical composition of four samples (7932, 7933-A, 7933-D and 7936) was determined at the universities of Oviedo (major elements) and Huelva (trace elements), Spain. Major elements were analyzed by X-ray fluorescence (XRF) with a Phillips

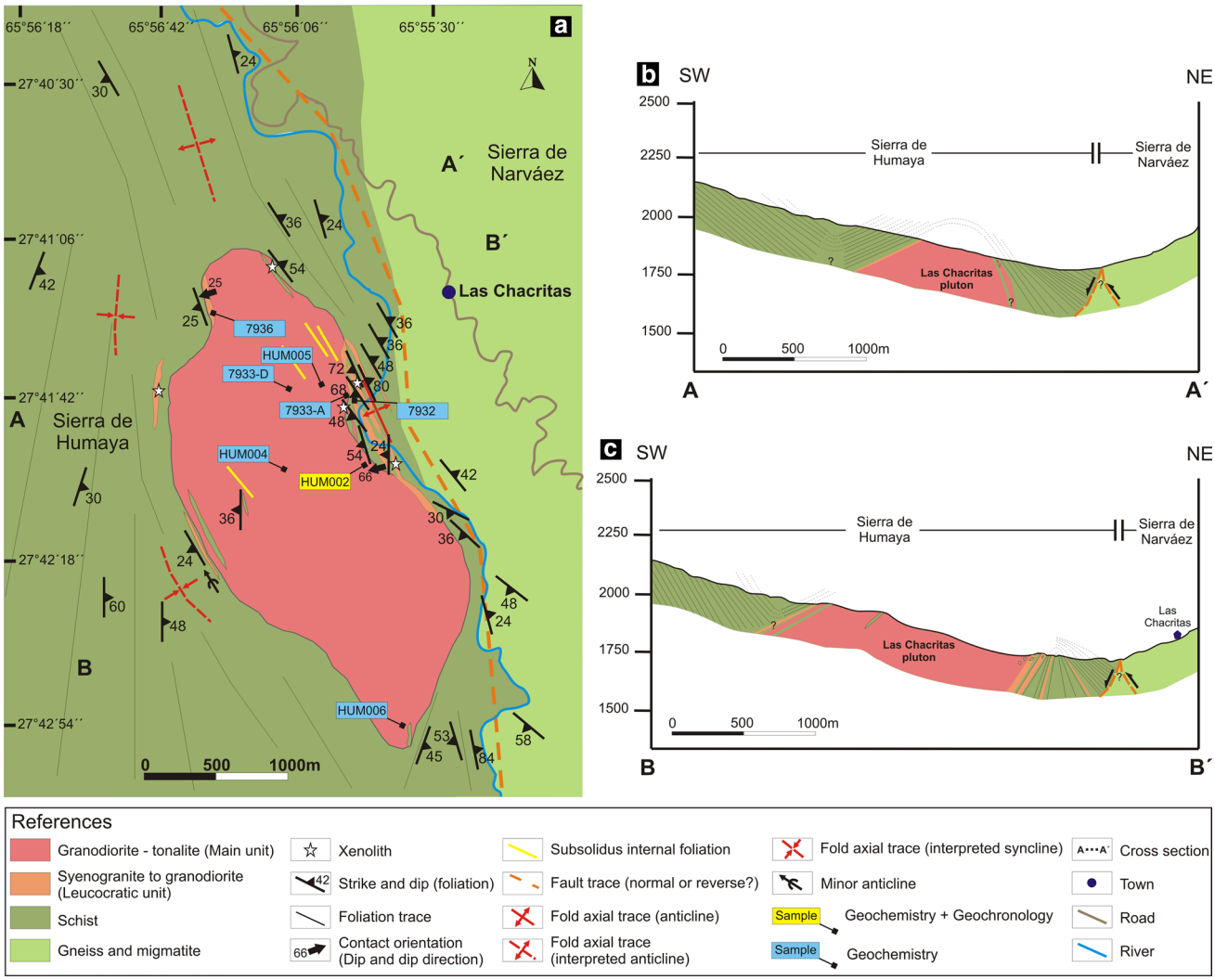

Fig. 2 **a** Geological map and **b**, **c** cross sections of the LCP with orientations of pluton-host rocks contacts, trends of folds and foliation in the host rocks

PW2404 system, using glass beads and yielding a precision better than ±1.5 %. Trace elements were analyzed by inductively coupled plasma mass spectrometry (ICP-MS) with a HP-4500 system. The Reference Standard Material was SARM1 (granite) in the Q&C procedure. % RSD was in the range of 14–20 %. Details on the procedures are given in de la Rosa et al. (2001). Additionally, geochemical analysis of samples HUM002, HUM004, HUM005 and HUM006 were carried out in Alex Stewart (Assayers) Argentina S.A. Major and trace elements were analyzed by inductively coupled plasma optical emission spectrometry (ICP-OES) following the procedures of Murray et al. (2000). Rare-earth elements (REEs) were analyzed by ICP-MS. Low Zr concentrations measured in both laboratories could be biased due to low-pressure dissolution used in analytical procedures.

The Las Chacritas pluton: field relationships, petrography and mineral chemistry

Field geology: lithology and structure

The igneous rocks

The LCP is an elongated, nearly elliptical body in map view exposed in the northern region of the Sierra de Humaya, which intruded into the medium-grade metamorphic rocks of El Portezuelo metamorphic–igneous complex. The pluton is about 4 × 1.5 km, with the long axis trending NNW (Fig. 2a). The main plutonic unit is a light gray, equigranular, medium-grained two-mica granodiorite to tonalite (Fig. 3a). NNW-striking pluton wall contacts dip 25°–66° to the west, except in the NE part of the pluton where they dip to the east (Fig. 2b, c). In the north-central

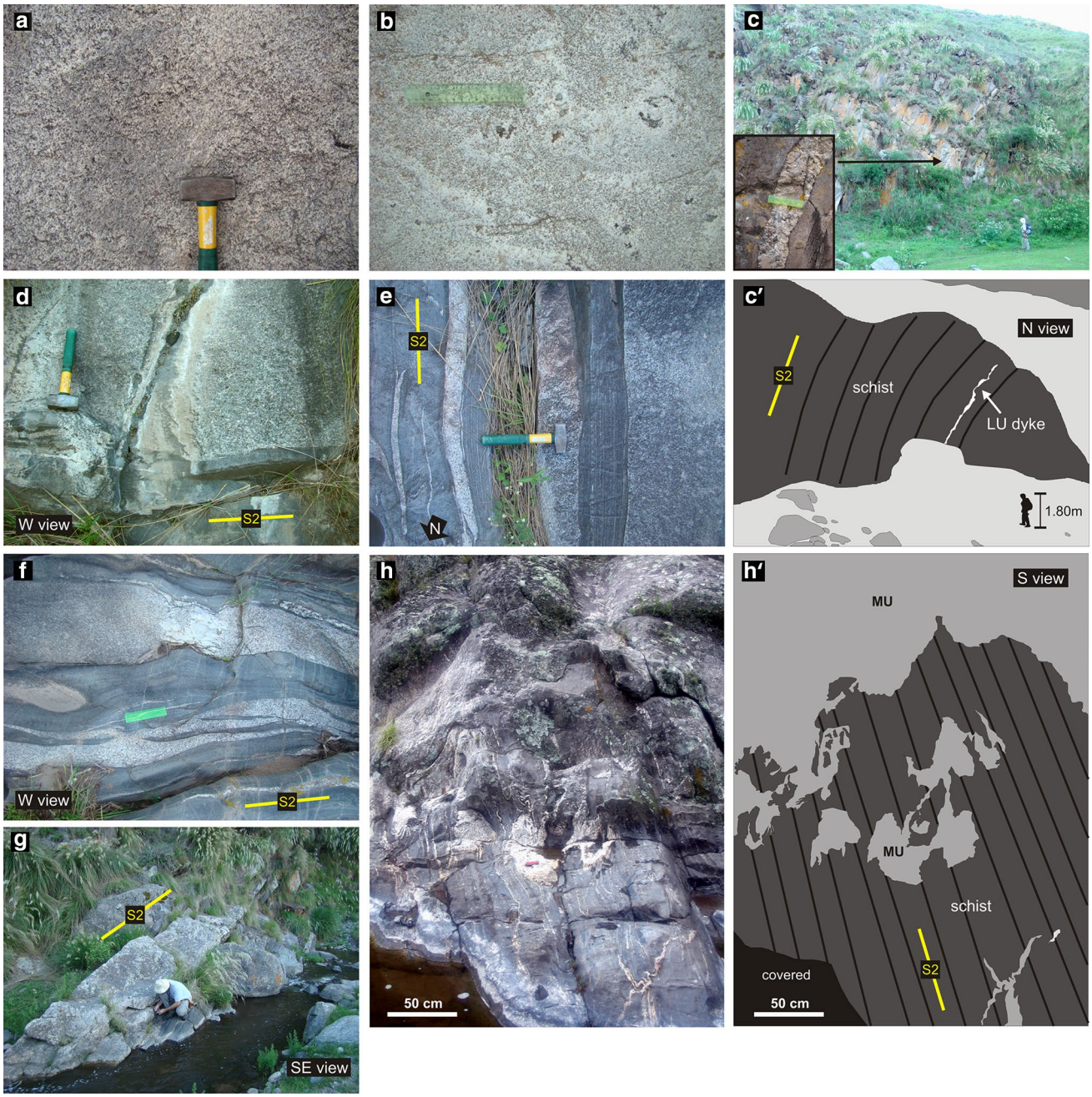

Fig. 3 **a** Two-mica granodiorite to tonalite of the main plutonic unit. **b** Muscovite-bearing syenogranite to granodiorite of the leucocratic unit. **c**, **c′** Outcrop-scale folding of the host rock metamorphic foliation in the border zone. A concordant sheet of the leucocratic unit (LU) is also gently folded evidencing syntectonic magmatism. A zoom of the sheet is visible in lower left corner of c. **d** Sharp and straight contact between the LCP and the wall rock. **e** Meso-scale sheeted contact characterized by alternation between concordant igneous units and metamorphic wall rocks. **f** Concordant granitic bodies of the main igneous unit containing sheeted host rock xenoliths. **g** Concordant leucocratic sheet intruding metasedimentary host rocks. **h**, **h′** Discordant contact between the main igneous unit (MU) and metasedimentary host rocks. Note disaggregation of the wall rock

part of the pluton, there are discrete ductile shear zones (a few tens of meters) with variable strain and characterized by the development of incipient S–C structures. These shear zones display NNW–SSE strikes that are nearly parallel to the schistosity of the metamorphic host rocks. No magmatic foliation was observed. On the margin of the pluton, a subordinate igneous unit is formed by leucocratic equigranular medium- to coarse-grained muscovite-bearing syenogranite to granodiorite (Fig. 3b). This unit occurs as concordant meter-scale sheets within the host rock or as

parallel to subparallel meter-scale border zones in sharp and straight internal contact with the main igneous unit of the pluton.

The host rocks

The host rocks are two-mica schist with a metamorphic foliation (S_2) defined by a differentiated layering that strikes NNW–SSE. At map scale, the LCP boundary is generally concordant with the host rocks S_2 fabric, which roughly drapes around the pluton, although in some parts, the host rock fabric in map view is truncated by the pluton. At depth, crosscutting relationships between pluton and host rock S_2 fabric are supposed from downward pluton projections (Fig. 2b, c). The orientations of the host rock foliation are shown in Figs. 1, 2, 4. The structural data have been divided into two domains: (1) the "LCP domain" restricted to the pluton's host rock aureole (i.e., map area of Fig. 2) and (2) the "regional domain" which includes the northern region of the Sierra de Humaya, i.e., the map area of Fig. 1, outside the LCP domain. In the LCP domain, onefold set was mapped, wherein the NNW-striking foliations S_2 dip toward the ENE and WSW, suggesting hectometer- to kilometer-scale local folding of the S_2 foliation. Here, we present (1) On the central-eastern contact zone, a NE–SW cross section that shows that the ENE-dipping S_2 fabric gradually steepens toward the pluton until vertical and then dips WSW, suggesting an F_3 close antiform (Fig. 2c). Outcrop-scale gentle folding has been observed in this WSW-dipping foliation (Fig. 3c, c′). (2) On the western contact zone, a synform is defined by the form of S_2 foliation planes (Fig. 2b, c). Locally, minor folds (centimeter-scale) were observed in this part of the contact with fold axis trending NNW–SSE. (3) At the northern end of the pluton, an open antiform is inferred because the S_2 foliation dips in the opposite direction (Fig. 2b). All inferred fold axis trends lie nearly parallel to the strikes of the S_2 foliation. It is important to note that W-dipping and folding of the S_2 foliation in the northern region of Sierra de Humaya is restricted to zones near the LCP (i.e., the LCP domain). In contrast, the regional domain shows a more uniform E-dipping S_2 foliation with average strike and dip of 0°, 36°E, respectively. The average N–S strike of S_2 in the regional domain slightly differs from the average NNW–SSE strike in the LCP domain.

Contact features and xenoliths

The contacts between the LCP and the wall rock are intrusive, i.e., injected type (Fig. 3d). They grade from undisturbed host rock passing through a zone defined by an increasing number of concordant sheets (from tens of cm up to 5 m thick and with compositions of both igneous units) to the plutonic rock containing host rock xenoliths (Fig. 3e–g). This concordant lithological alternation characterizes a sheeted border zone. Locally, discordant contacts are observed (Fig. 3h, h′). In the central-eastern part of the border zone, some concordant sheets show the same deflection as the folded host rock foliation (Fig. 3c, c′). Some irregular branch-like discordant granitic dykes crosscut the S_2 foliation through fractures and generate local meter-scale gentle folds (Fig. 5a, a′). In this zone, symmetric lens-shaped apparent boudins of leucocratic composition (see structure definition in Bons et al. 2004) are developed in the host at high angles with the S_2 foliation and the pluton–wall rock contact (Fig. 5b, b′).

Xenoliths of wall rock occur within the pluton, mainly near the contacts. Larger xenoliths (tens of meters) in the central-western part of the LCP were recognized (Fig. 2a, c). Some rotated wall rock xenoliths (i.e., where xenolith foliation is at high angle to S_2 and thus defined as stoped blocks) with angular shapes are present in the leucocratic sheets (Fig. 5c, c′) and within the pluton near the contact. In the granitic sheets, small sheeted xenoliths are parallel to the attitude of the intrusive bodies and the wall rock foliation (S_2) (Fig. 3f). Disaggregation of the metasedimentary rocks is observed in the wall rock and xenoliths (Figs. 3h, h′, 4, 5c, c′).

Petrography and mineral chemistry

The two-mica granodiorite to tonalite of the main plutonic unit has an allotriomorphic inequigranular texture (Fig. 6a) and consists of plagioclase (31–49 %); quartz (30–46 %); microcline (0–14 %); muscovite (6–12 %); biotite (5–11 %); and <2 % apatite, monazite, zircon and epidote as accessories (modal proportions for 5 samples). Representative compositions of minerals are presented in tables in the Electronic Supplementary Material. Plagioclase occurs as anhedral to subhedral crystals, with polysynthetic twinning and often altered to sericite and muscovite. Twinning in plagioclase controls the $muscovite_2$ direction growth (Fig. 6b). Some crystals exhibit sericite-altered cores and fresh border zones (Fig. 6c). Plagioclase shows concentric extinction of compositional zoning (oscillatory zoning) (Fig. 6b, c). In all cases, An contents range from 20 to 30 mol% ($n = 14$). Quartz occurs as anhedral crystals, with typical undulatory extinction and slight subgrain development. Microcline (Or_{90-94}) is interstitial and exhibits myrmekite development at plagioclase contacts. Muscovite is observed in two main forms: (1) as larger, primary subhedral laths ($muscovite_1$) forming part of the matrix (Fig. 6a) and (2) as smaller euhedral to subhedral secondary laths ($muscovite_2$) associated with plagioclase (Fig. 6b, c). Low MgO (avg. 0.72 wt%) and SiO_2 (avg. 44.53 wt%) contents in $muscovite_1$ support its primary magmatic origin (Fig. 7;

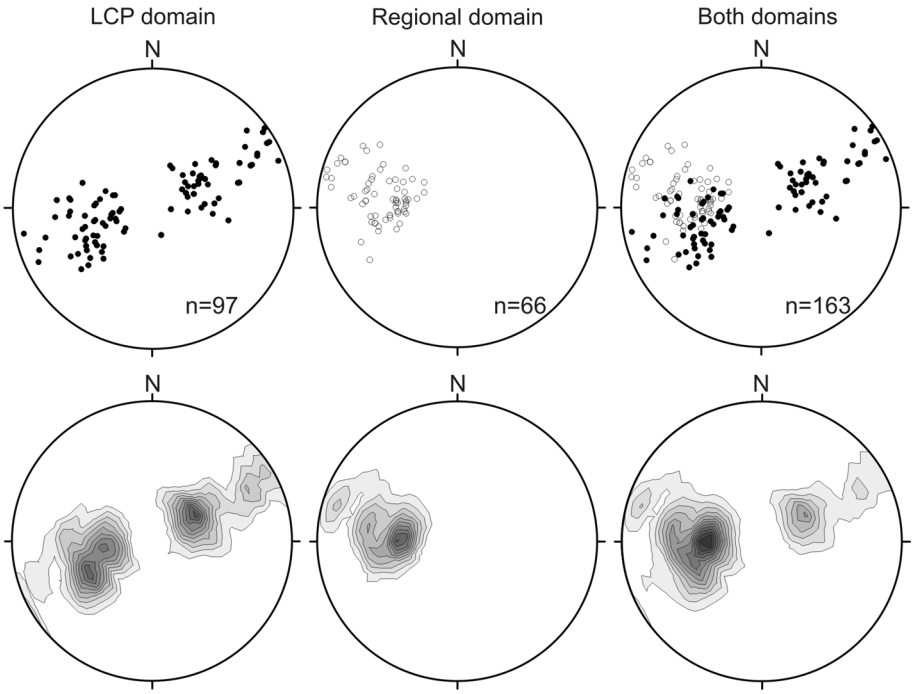

Fig. 4 Equal area projections on the lower hemisphere show poles of the S_2 metamorphic foliations as separated by structural domains. Density stereograms are also displayed

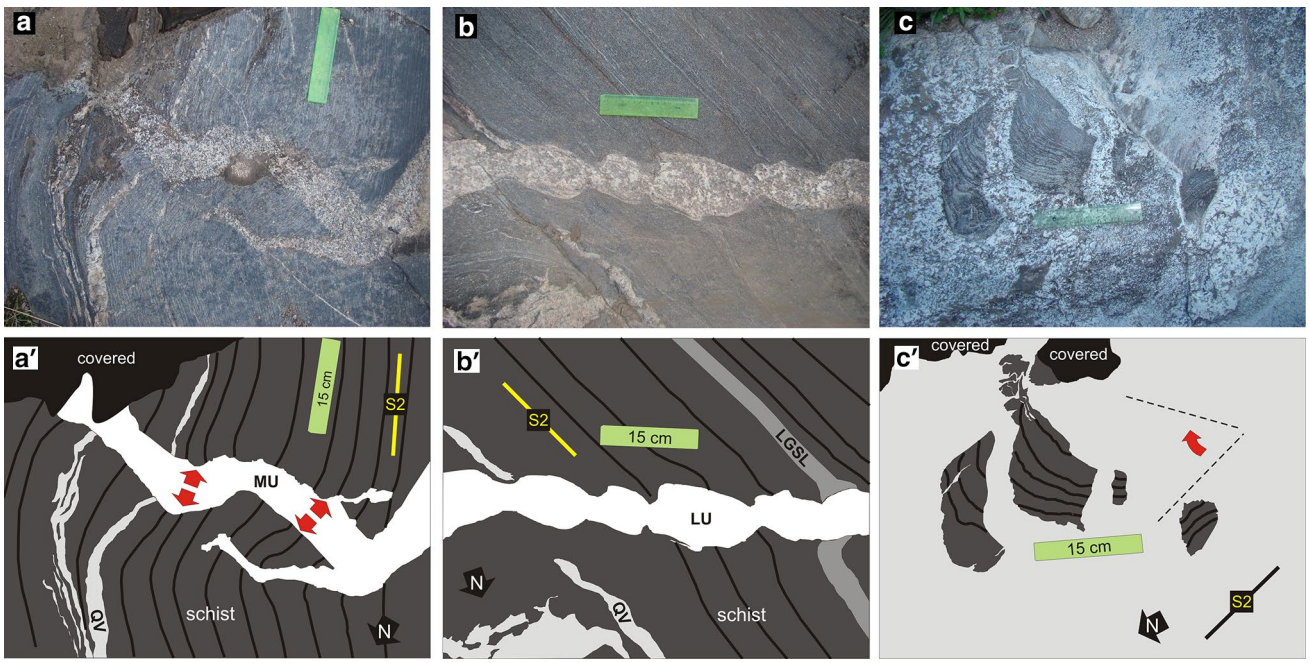

Fig. 5 **a**, **a′** Irregular discordant granitic dykes crosscutting the S_2 foliation by fractures and generating meter-scale local gentle folds. *MU* main igneous unit, *QV* quartz vein. *Red arrows* indicate opening direction of the fracture and local shortening direction over the host rock. **b**, **b′** Symmetric lens-shaped apparent boudins of leucocratic composition showing high angle orientation with the S_2 foliation. A reference layer (LGSL) is highlighted in (**b′**); *LGSL* light gray schist layer. **c**, **c′** Rotated xenoliths with angular shapes hosted in leucocratic sheets. *Red arrow* indicates the rotation sense. Note disaggregation of the xenoliths

Miller et al. 1981). Biotite occurs as subhedral to anhedral crystals, and the main accessory phases (apatite, monazite, zircon and epidote) are commonly associated with it. Biotite has an X_{Mg} of 0.34–0.36 and Ti contents ranging from 0.36 to 0.42 per double formula unit (d.f.u.). Microscopically, subsolidus deformation related to ductile shearing is evidenced by a weakly spaced anastomosing foliation characterized by rough-to-smooth mica-rich cleavage domains

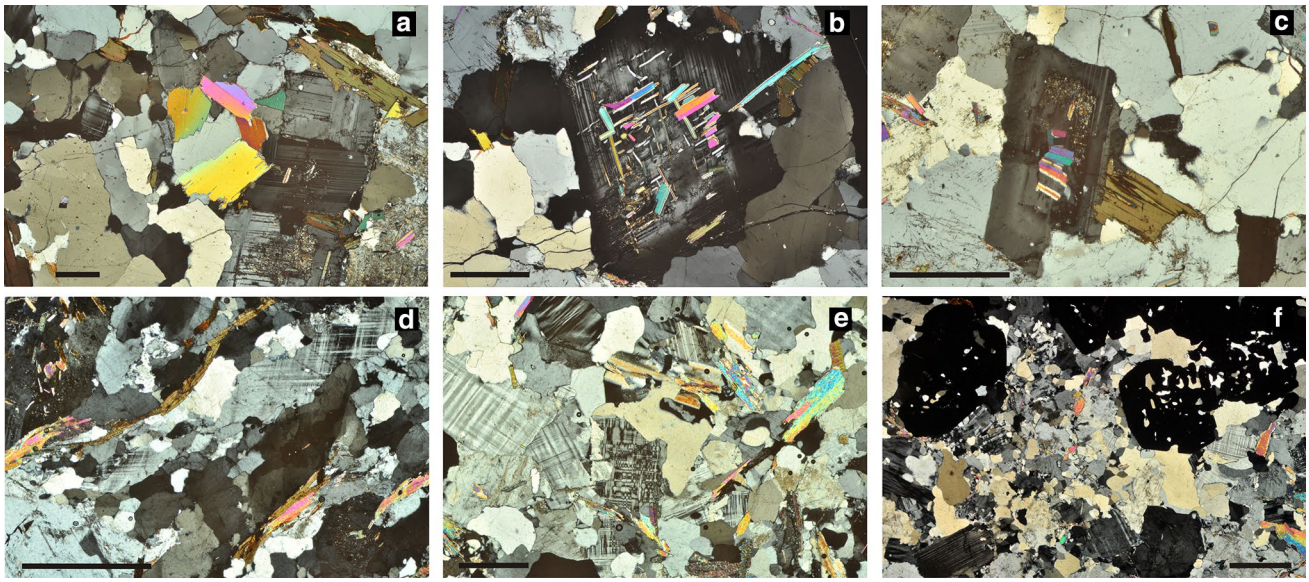

Fig. 6 From **a** to **d** photomicrographs of the main igneous unit. **a** Texture and mineralogy of a two-mica granodiorite. Large subhedral laths of muscovite$_1$ are shown in the center of the photomicrograph. **b** Compositional zoning in plagioclase crystal. Direction growth of muscovite$_2$ is controlled by twinning in plagioclase. **c** Altered cores and fresh borders in zoned plagioclase. **d** Deformed granitoid showing a weak spaced foliation characterized by minerals elongated in the same direction. **e**, **f** Photomicrographs of the leucocratic unit. **e** Magmatic texture and mineralogy of a monzogranite. **f** Poikilitic garnet forming garnet-clusters in a monzogranite. *Scale bars* 1 mm

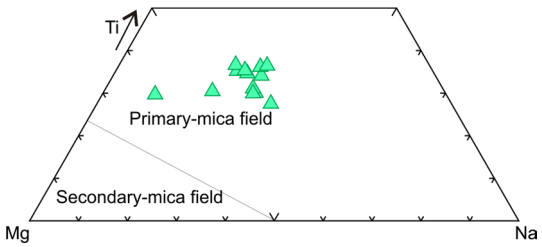

Fig. 7 Plotted compositions of white micas texturally interpreted to be of primary origin on the Mg–Ti–Na diagram. The limits between secondary and primary muscovite are from Miller et al. (1981)

and microlithons composed mostly of quartz, plagioclase and microcline (Fig. 6d). All minerals are elongated in the same direction and often display undulatory extinction, and some muscovite and plagioclase crystals are lensoidal.

The leucocratic muscovite-bearing granitoids (i.e., the leucocratic igneous unit) have an allotriomorphic inequigranular texture and consist of microcline (13–37 %), plagioclase (18–33 %), quartz (26–43 %), muscovite (13–25 %) and biotite (<1 % modal proportions, $n = 4$), with tourmaline, garnet, oxides and apatite as accessories (Fig. 6e). Microcline occurs as anhedral crystals with tartan twinning and sometimes shows irregular and patchy microperthites. Inclusions of plagioclase, apatite, muscovite and quartz are observed occasionally. Plagioclase is anhedral to subhedral and slightly altered to kaolinite and sericite, with scarce inclusions of apatite and muscovite. Quartz is anhedral, with undulatory extinction and slight subgrain development. Muscovite occurs as subhedral grains and tiny needle-shaped crystals, assumed to be of primary origin. Biotite is scarce and occurs as anhedral crystals. Garnet is euhedral and poikilitic with inclusions of quartz, and tends to amalgamate in garnet clusters (Fig. 6f).

Whole-rock chemical composition

Major elements

Representative samples of the main igneous unit of the LCP are felsic or evolved in composition (SiO_2 from 71 to 74 wt%, $n = 6$) (Fig. 8; Table 1). They are enriched in CaO (1.6–3 wt%) and Na_2O (3.2–3.8 wt%, with a K_2O/Na_2O ratio <1). The granitoids are rich in FeO^{tot} (2.1–2.9 wt%) relative to MgO with high $FeO^{tot}/(FeO^{tot} + MgO)$ ratios (0.78–0.83). Following the classification scheme of Frost et al. (2001), the compositions plot in the magnesian field but close to the limit with the ferroan field (Fig. 9a), and some samples fall in the latter. In the modified alkali-lime index, these samples are dominantly calcic (Fig. 9b). They are slightly peraluminous with an alumina saturation index (ASI) of 1.07–1.19. On Harker variation diagrams, the main igneous facies show a decrease in TiO_2, FeO^{tot}, MgO and CaO, and an increase in of SiO_2, whereas K_2O and Na_2O have gently positive correlations (Fig. 8).

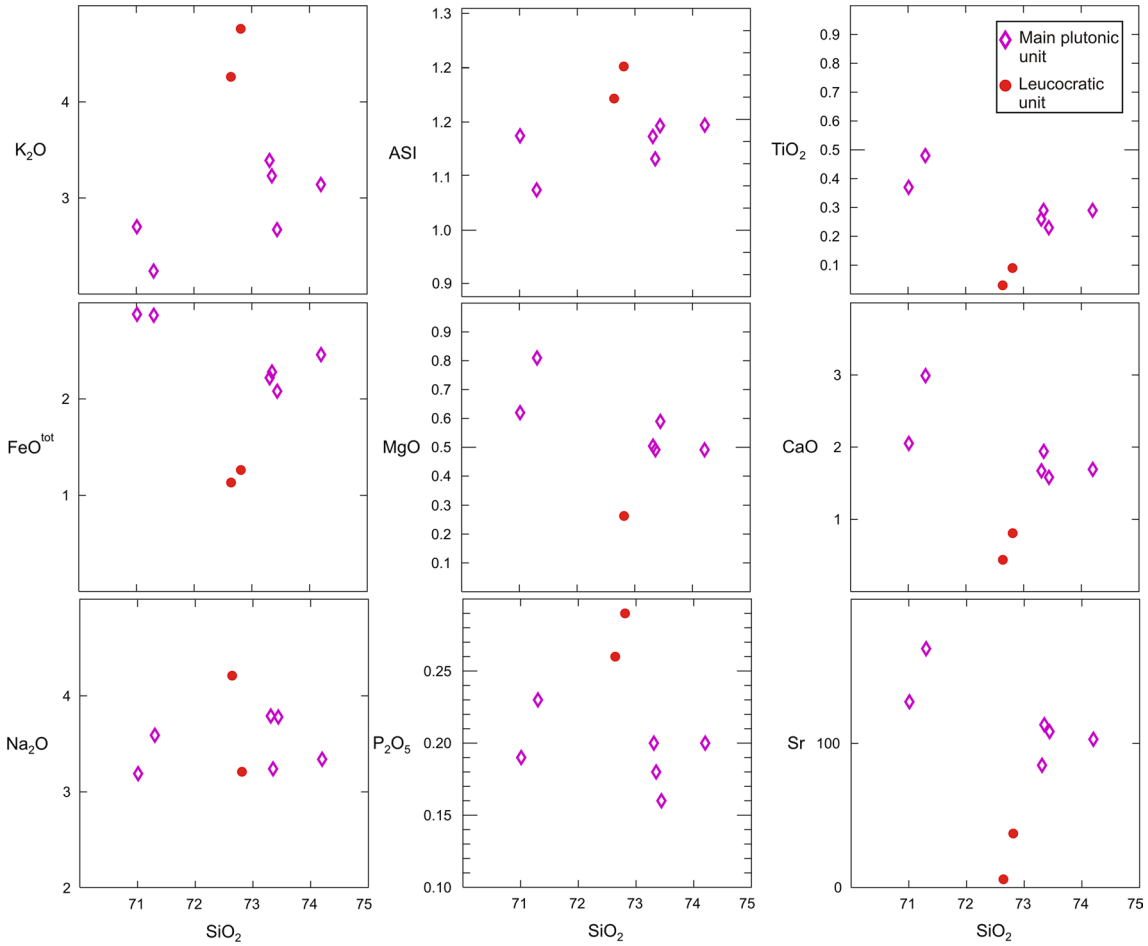

Fig. 8 Harker variation diagrams for the studied granitoids. ASI versus SiO_2 diagram is also shown

The leucocratic igneous unit is also felsic ($SiO_2 \approx 73$ wt%, $n = 2$) but moderately peraluminous (ASI = 1.24–1.30). They are depleted in CaO (<1 wt%) but enriched in alkalis (≈8, with a K_2O/Na_2O ratio ≥1). They plot with magnesian and alkali-calcic granitoids (Fig. 9a, b). On Harker variation diagrams, they exhibit a widespread depletion in the major oxides (excluding alkalis and P_2O_5) deviating from the main igneous trend (Fig. 8). On the A–B diagram after Villaseca et al. (1998), the main igneous unit is distinguished as low-to-moderately peraluminous, whereas the leucocratic unit is felsic and peraluminous (Fig. 10).

Trace elements

A trace element bulk earth-normalized plot is shown in Fig. 11a. The granitoids of the main igneous unit exhibit high contents of large ion lithophile elements (Cs, Rb, Ba and K), incompatible elements (Th, La, Ce and Nd) and even relatively high Y and Yb. In contrast, the leucocratic granitoids have a strong depletion of most of the elements with the exception of Cs, Rb and K (all of these hosted in K-feldspar). The leucocratic granitoids show lower Y content than the granitoids of the main igneous unit.

Chondrite-normalized REE patterns show that the main igneous unit has relatively high LREE and low HREE values [$(La/Yb)_N = 7.62–14.41$], with moderately negative Eu anomalies (Eu/Eu* = 0.56–0.70) (Fig. 11b). Leucocratic igneous samples are depleted in REE (Fig. 11b; Table 1), with a flat pattern [$(La/Yb)_N = 1.71–1.88$] and variable negative Eu-anomalies (Eu/Eu* = 0.26–0.70).

Monazite EPMA geochronology

Sample HUM002 was analyzed for in situ U–Th–Pb dating of monazite. The data set for this sample includes 28 spots measured in 16 monazite grains. Electron microprobe data for analyzed monazites and calculated ages are reported in Table 2. Monazite occurs as euhedral and subhedral grains, prismatic or equant, and is typically less than 70 μm long. Some anhedral grains were also observed. Monazite crystals appear mainly as inclusions in biotite, muscovite, quartz,

Table 1 Whole-rock major and trace element geochemistry of the Las Chacritas pluton

Unit	Main plutonic unit								Leucocratic unit			
Rock	Tonalite	Granodiorite	Tonalite	Granodiorite	Granodiorite	Granodiorite			Monzogranite	Granodiorite		
Sample number	7933-A	7933-D	HUM002[a]	HUM004[a]	HUM005[a]	HUM006[a]	Average	SD	7932	7936	Average	SD
Major oxides (wt%)												
SiO_2	73.44	73.31	71.01	73.35	74.20	71.30	72.77	1.30	72.81	72.64	72.73	0.12
Al_2O_3	13.83	14.51	13.33	13.48	13.67	14.12	13.82	0.43	14.64	14.51	14.58	0.09
Fe_2O_3 (T)	2.31	2.47	3.20	2.54	2.74	3.19	2.74	0.38	1.41	1.26	1.33	0.10
MnO	0.06	0.05	0.05	0.04	0.05	0.05	0.05	0.00	0.05	0.09	0.07	0.03
MgO	0.59	0.50	0.62	0.49	0.49	0.81	0.58	0.12	0.26	nd	0.26	nd
CaO	1.58	1.67	2.05	1.94	1.69	2.99	1.99	0.52	0.81	0.44	0.63	0.26
Na_2O	3.78	3.79	3.19	3.24	3.34	3.59	3.49	0.27	3.21	4.21	3.71	0.71
K_2O	2.67	3.39	2.70	3.23	3.14	2.24	2.90	0.43	4.76	4.26	4.51	0.35
TiO_2	0.23	0.26	0.37	0.29	0.29	0.48	0.32	0.09	0.09	0.03	0.06	0.04
P_2O_5	0.16	0.20	0.19	0.18	0.20	0.23	0.19	0.03	0.29	0.26	0.27	0.02
LOI	0.67	0.59	1.05	0.65	0.65	1.02	0.77	0.21	0.83	0.73	0.78	0.07
Total	99.31	100.74	97.75	99.43	100.49	100.02	99.62	1.08	99.14	98.44	98.79	0.50
Trace elements (ppm)												
Li	42	51	40	49	73	34	48	14	25	21	23	3
Sc	4.8	3.4	5.9	5.2	4.8	5.4	4.9	0.9	2.9	1.2	2.0	1.2
Be	4	3	nd	nd	nd	nd	4	1	3	5	4	1
V	18	16	25	19	19	42	23	10	4	4	4	0
Cr	28	16	7	5	6	12	12	9	21	21	21	0
Co	4	2	4	3	2	5	3	1	1	1	1	0
Ni	18	10	6	4	5	13	9	6	10	11	10	1
Cu	19	10	17	17	17	15	16	3	10	13	12	2
Zn	61	57	54	49	47	55	54	5	32	48	40	12
Ga	25	24	16	16	15	18	19	4	16	16	16	0
As	2	1	bdl	bdl	bdl	bdl	1	1	1	1	1	0
Rb	88	94	nd	nd	nd	nd	91	4	112	144	128	23
Sr	108	85	129	113	103	166	117	28	37	6	22	22
Y	24.2	18.6	27.2	26.4	23.0	24.1	23.9	3.0	8.1	3.6	5.9	3.1
Zr	51	34	27	21	26	27	31	11	19	19	19	1
Nb	10	9	7	7	7	7	8	1	11	14	12	2
Mo	5	4	4	3	4	2	4	1	4	3	4	0
Cs	9	8	nd	nd	nd	nd	9	1	4	8	6	2
Ba	250	278	517	529	425	322	387	121	79	13	46	46
La	30.7	22.5	38.5	34.0	31.4	46.8	34.0	8.2	3.0	1.2	2.1	1.2
Ce	67.5	47.0	88.3	72.3	63.7	93.1	72.0	16.9	6.9	3.0	5.0	2.8
Pr	8.2	5.8	9.6	8.1	7.3	11.1	8.3	1.8	0.8	0.4	0.6	0.3
Nd	29.5	22.7	38.0	31.6	28.9	42.9	32.3	7.2	3.1	1.3	2.2	1.2
Sm	5.8	4.6	7.0	6.6	6.3	8.1	6.4	1.2	0.9	0.5	0.7	0.3
Eu	1.0	1.0	1.6	1.5	1.3	1.8	1.3	0.3	0.2	0.0	0.1	0.1
Gd	5.2	4.5	7.1	6.3	5.4	8.4	6.1	1.4	1.1	0.6	0.8	0.3
Tb	0.8	0.7	1.2	1.1	0.9	1.2	1.0	0.2	0.2	0.1	0.2	0.1
Dy	4.7	3.9	5.1	5.4	4.2	5.1	4.8	0.6	1.5	0.8	1.1	0.5
Ho	1.0	0.8	0.9	1.0	0.6	0.9	0.9	0.1	0.3	0.1	0.2	0.1
Er	2.7	2.1	3.5	3.0	2.4	2.9	2.8	0.5	0.9	0.4	0.6	0.4

Table 1 continued

Unit	Main plutonic unit								Leucocratic unit			
Rock	Tonalite	Granodiorite	Tonalite	Granodiorite	Granodiorite	Granodiorite			Monzogranite	Granodiorite		
Sample number	7933-A	7933-D	HUM002[a]	HUM004[a]	HUM005[a]	HUM006[a]	Average	SD	7932	7936	Average	SD
Tm	0.4	0.3	0.3	0.4	0.3	0.3	0.3	0.1	0.2	0.1	0.1	0.1
Yb	2.7	1.8	2.4	2.7	2.1	2.2	2.3	0.3	1.1	0.5	0.8	0.4
Lu	0.4	0.3	0.3	0.4	0.2	0.3	0.3	0.1	0.2	0.1	0.1	0.1
Ta	1.2	1.3	bdl	bdl	bdl	bdl	1.2	0.1	1.5	2.9	2.2	1.0
Pb	25	19	14	20	22	24	21	4	27	14	21	9
Th	15	11	14	bdl	bdl	14	14	2	1	1	1	0
U	3.0	1.3	bdl	bdl	bdl	bdl	2.1	1.2	1.3	1.0	1.2	0.2
REE totals	160.6	117.9	203.7	174.3	155.0	255.1	177.8	47.0	20.4	9.1	14.8	8.0
FeO^{tot}	2.08	2.22	2.88	2.28	2.46	2.87	2.46	0.34	1.26	1.13	1.20	0.09
ASI	1.19	1.17	1.17	1.13	1.19	1.07	1.15	0.05	1.30	1.24	1.27	0.05

LOI loss on ignition, *nd* not determined, *bdl* below detection limit, *ASI* aluminum saturation index, *FeO^{tot}* ferrous oxide

[a] Analysis carried out in Alex Stewart Argentina S.A

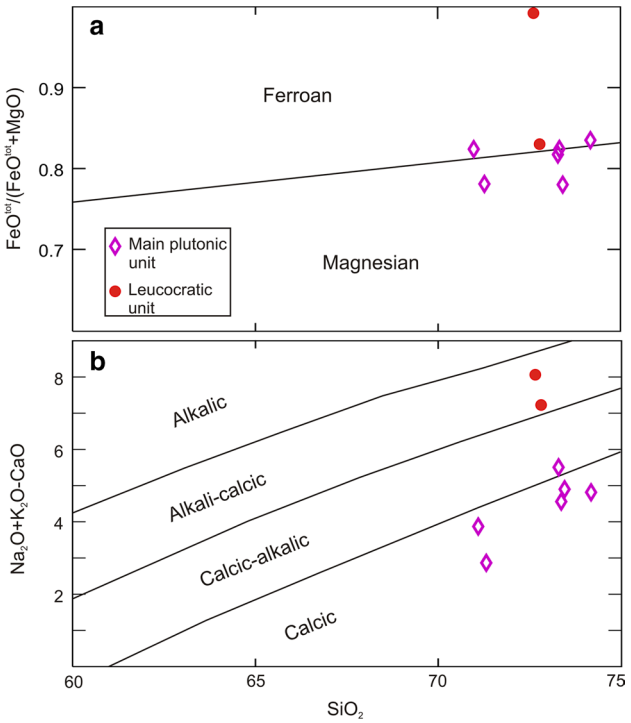

Fig. 9 Studied granitoids plotted on the classification diagrams of Frost et al. (2001): **a** $FeO^{tot}/(FeO^{tot} + MgO)$ versus SiO_2, (wt %) and **b** $Na_2O + K_2O$–CaO versus SiO_2, (wt%)

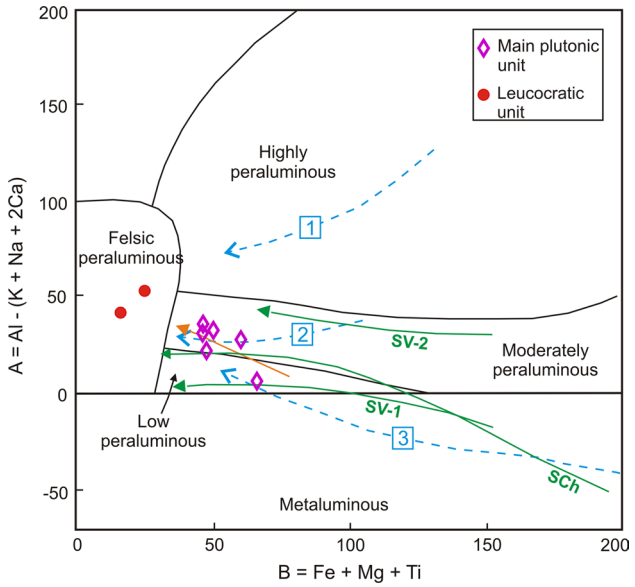

Fig. 10 **a** A–B diagram of Debon and Le Fort (1983) modified from Grosse et al. (2011) for the studied granitoids. Granitoid compositional fields are from Villaseca et al. (1998). *Solid orange arrow* is the hypothetical trend defined by the main plutonic unit. *Solid green arrows* are the trends of natural series: SCh, I-type granitoids of the Sierra de Chepes (Dahlquist et al. 2005); SV-1, I-type granitoids and SV-2, transitional I/S-type granitoids of the Sierra de Velasco (Grosse et al. 2011). *Dashed blue arrows* are trends of experimental melts from different protoliths: 1 = pelite-derived melt (Vielzeuf and Holloway 1988); 2 = graywacke-derived melt (Conrad et al. 1988); 3 = amphibolite-derived melt (Beard and Lofgren 1991)

K-feldspar and plagioclase. Backscatter electron images show compositional zoning in some monazite crystals (Fig. 12a). Monazite domains with high brightness in BSE images are consistent with lower Y contents (Fig. 12b). All grains show significant variations in U contents and Th/U ratios.

Calculated dates spread from 522 to 461 Ma. Top-down approach monazite analysis strategy (Williams et al. 2006) based on the age histogram method (Montel

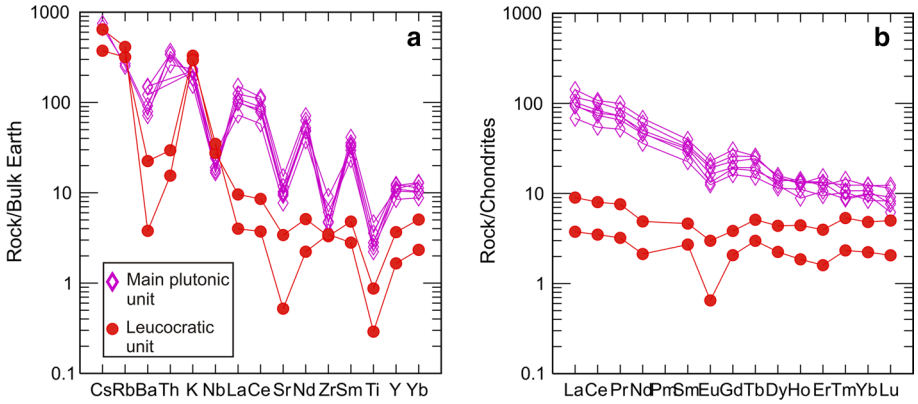

Fig. 11 **a** Bulk earth-normalized trace element patterns for selected samples (normalizing values from Hickey et al. 1986). **b** Chondrite-normalized patterns for selected samples (normalizing values from Nakamura 1974)

Table 2 Monazite composition and geochronologic data for sample HUM002

Analysis number	Date cluster	Y_2O_3 (wt%)	PbO (wt%)	ThO_2 (wt%)	UO_2 (wt%)	Th/U	Date (Ma)	1 sigma (Ma)
HUM2Mz1	I	1.42	0.105	5.09	0.05	103.85	470.4	8.9
HUM2Mz2	II	3.47	0.119	5.07	0.13	38.75	510.3	9.8
HUM2Mz3c	I	1.11	0.098	4.60	0.06	79.85	484.0	9.1
HUM2Mz3r	II	1.44	0.115	5.25	0.05	98.04	499.9	9.2
HUM2Mz3r	I	1.86	0.145	4.86	0.74	6.57	468.6	8.9
HUM2Mz4	I	2.19	0.118	4.93	0.26	18.99	481.7	9.2
HUM2Mz5	I	1.33	0.090	4.34	0.05	90.82	471.9	8.7
HUM2Mz6c	II	1.66	0.104	4.71	0.08	61.81	494.2	9.2
HUM2Mz6r	I	1.33	0.102	4.89	0.05	107.28	478.0	9.1
HUM2Mz7c	I	2.69	0.124	5.03	0.32	15.51	480.8	8.9
HUM2Mz7r	I	1.50	0.098	4.80	0.06	75.91	462.9	8.7
HUM2Mz8c	II	2.45	0.111	5.05	0.10	50.32	488.5	9.2
HUM2Mz8r	I	2.05	0.111	5.09	0.09	54.64	485.8	8.9
HUM2Mz9	II	3.74	0.132	5.64	0.17	33.09	501.8	9.4
HUM2Mz10	II	2.83	0.127	4.99	0.22	22.49	521.7	10.2
HUM2Mz11c	I	1.60	0.101	4.75	0.06	82.13	482.5	8.8
HUM2Mz11r	I	1.77	0.094	4.44	0.10	44.65	465.9	8.7
HUM2Mz12	I	2.09	0.104	4.85	0.09	55.22	476.4	9.1
HUM2Mz13	I	1.53	0.101	5.00	0.05	94.43	461.2	8.7
HUM2Mz14c (P2)	I	1.65	0.106	5.06	0.06	82.22	473.5	9.2
HUM2Mz14r (P4)	I	1.72	0.109	4.73	0.26	18.47	461.3	8.7
HUM2Mz14c (P1)	I	1.50	0.100	4.81	0.06	82.12	473.0	9.0
HUM2Mz14r (P3)	II	2.33	0.108	4.61	0.17	27.68	495.0	9.3
HUM2Mz15	I	1.80	0.134	4.05	0.83	4.87	466.6	9.0
HUM2Mz16c	I	1.04	0.086	4.26	0.04	105.77	462.6	8.7
HUM2Mz16r	I	1.48	0.100	4.79	0.07	71.75	473.5	8.8
HUM2Mz16r	I	1.24	0.092	4.37	0.05	89.72	481.8	8.8
HUM2Mz16r	I	1.56	0.136	4.39	0.74	5.97	472.0	8.9

Weighted mean age from first date cluster (I): 474.1 ± 4.3 Ma (2 sigma) ($n = 21$)

Weighted mean age from second date cluster (II): 502.7 ± 10 Ma (2 sigma) ($n = 7$)

P1, P2, P3 and P4 are spots in monazite grain 14 (see Fig. 12)

et al. 1996, 2000) yielded two main date clusters with weighted means of 474.1 ± 4.3 Ma (2σ; $n = 21$) and 502.7 ± 10 Ma (2σ; $n = 7$) (Fig. 13). The first date cluster is considered the best estimate for the magma crystallization. The age span of 25 Ma, from 486 to 461 Ma, of this coherent group could be attributed to partial inheritance

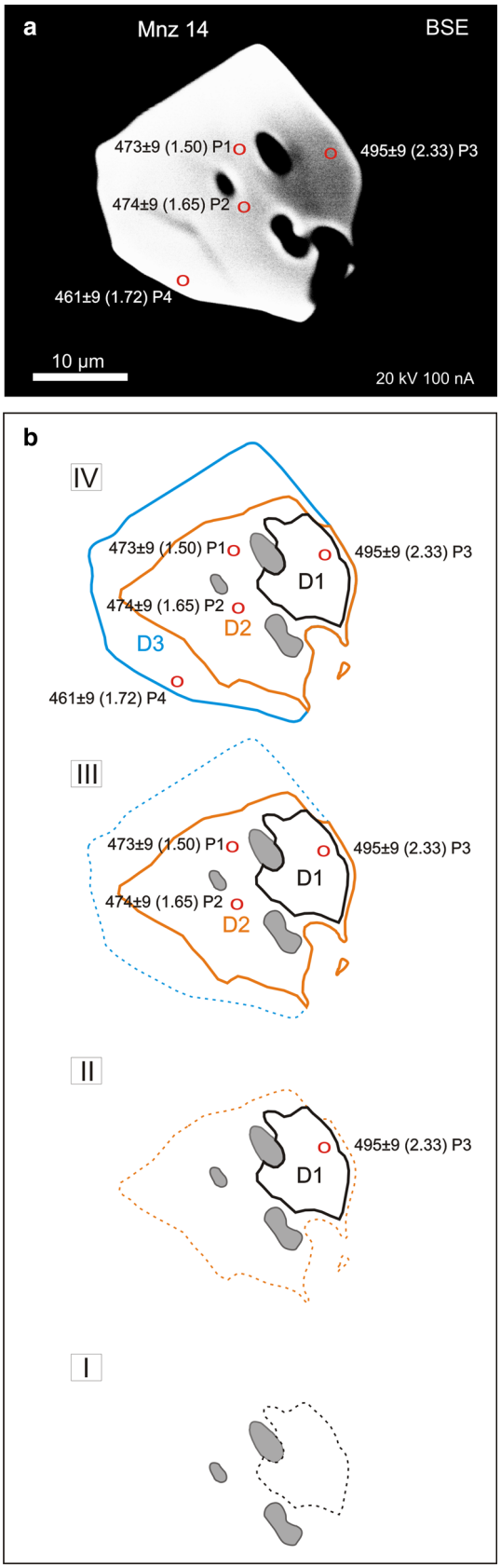

◀**Fig. 12** **a** Backscattered electron images showing compositional zoning in a monazite crystal (grain 14). **b** Illustration of monazite growth (grain 14). Three domains are interpreted on the basis of compositional and age differences. D_n domain number, P_n analyzed spot. The numbers in brackets are Yttrium values (wt%)

of older monazite, although this age range is within the 2σ analytical uncertainty of the individual results. The second date cluster is interpreted to be due to the existence of inherited crystals (xenocrysts or inherited cores). Importantly, Y content in the three oldest grains is high (>2.8 %; mean of cluster "$n = 7$" ~2.6 %) and consistent with Y content in grains from the high-grade metamorphic basement (~2.5 % "$n = 43$," unpublished work in progress). Detailed analyses of individual crystals in BSE images (similar method to the bottom-up approach of Williams et al. 2006) show several domains in monazite, with differences in age and chemical composition. Grain 14 exhibits concentric zoning from one of the sides, displaying three domains characterized by distinct Y and U content (Fig. 12). The inner domain ($D1_{14}$) displays an irregular shape and has higher Y and U contents (~2.33 wt% Y_2O_3, ~0.17 wt% UO_2) than the intermediate subhedral domain ($D2_{14}$;~1.57 wt% Y_2O_3, ~0.06 wt% UO_2 "$n = 2$"). The outer euhedral domain $D3_{14}$ has Y content of 1.72 % and the highest U content of 0.26 %. The domain $D1_{14}$ yields a date of 495 ± 9 Ma (1σ) which—together with the high Y content—represents the older date cluster (~502 Ma). Nearby dates (regarding analytical uncertainty) and similar Y content allow to group domains $D2_{14}$ (474 ± 9 Ma) and $D3_{14}$ (461 ± 9 Ma) into the younger date cluster (~474 Ma). Our data indicate that at least two monazite growth episodes are recorded in the LCP (i.e., the two main date clusters), which in turn, linked to U–Th-total Pb ages provide a detailed record of the geologic history of its host rock (Williams et al. 2007).

Discussion

Petrogenesis of the Las Chacritas pluton

Field observations, petrography, mineral chemistry and whole-rock compositions of the LCP suggest participation of the surrounding metasedimentary basement rocks in the genesis of the two distinct groups of silicic igneous rocks of the LCP, i.e., the main unit and the leucocratic unit. At first, the presence of disaggregated metasedimentary xenoliths directly indicates crustal contamination during magma emplacement. The main unit samples have concentrations of silica, alumina, and alkalis compatible with experimental melts produced by incongruent dehydration-melting of

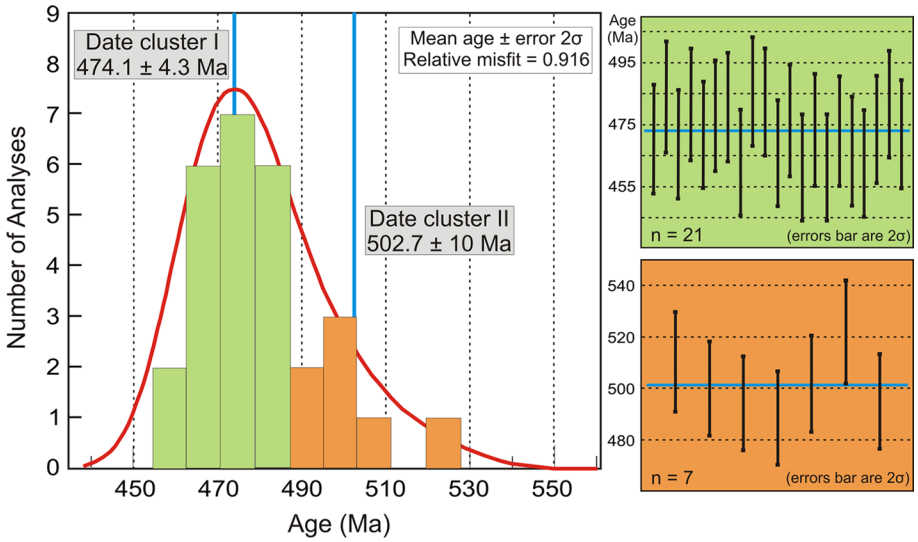

Fig. 13 Probability density plots with histograms for monazite EPMA age data and weighted average age plots from date cluster I and II

mica + quartz (e.g., Patiño Douce 1999). This interpretation is consistent with the presence of primary muscovite in them (Fig. 7), which is an indicator of peraluminous magmas (Speer 1984). In fact, the generally accepted intersection of the granite solidus curve with the experimental curves for the reaction Ms + Qtz = Kfs + Al-silicates + H_2O at approximately 3–4 kbar (Pattison and Tracy 1991) is consistent with the emplacement level of this pluton (~3.8 kbar; see below). Further, inherited monazite with higher Y contents of metamorphic origin (monazite date cluster II) supports the link between the LCP and its source terrains. However, the calcium content in the main unit of the LCP is too high. The fact that these calcic granitoids plot in the boundary between ferroan and magnesian granitoids is rare since ferroan calcic granitoids are unknown (Frost et al. 2001). On the A–B diagram, the samples of the main unit plot in the low and moderately peraluminous fields without a clear trend (Fig. 10). They fall between the trends of experimental melts and natural series (e.g., transitional I/S-type granitoids, Fig. 10), suggesting that more than one source of melt and/or processes were involved in the origin and evolution of the main unit of the LCP. In concordance, on major element diagrams from Patiño Douce et al. (1999), these samples plot in a restricted zone between the fields of metagraywacke- and amphibolite-derived melts (Fig. 14).

Harker diagrams of the leucocratic granitoids of the LCP presented above show that these diverge from the trend of the main igneous unit. Also their REE patterns are strongly LREE-depleted. According to their mineralogy (muscovite ± tourmaline ± garnet) and major element composition, they may correspond to pure crustal melts as a result of dehydration melting of muscovite-rich metasediments, i.e., the peraluminous leucogranites of Patiño Douce (1999) (Fig. 14). LREE-depleted patterns in the leucocratic granitoids are consistent with disequilibrium melting, where monazite and perhaps other accessory minerals did not partake in the muscovite dehydration-melting reactions that produced LREE-depleted melts (Nabelek and Glascock 1995). Low Y contents in leucocratic granitoids suggest incomplete monazite and/or xenotime participation in the generation of the leucogranites.

In summary, the origin and evolution of the LCP involved multiple melt sources. The main unit may be linked either with interaction of crustal rocks with mafic magmas or crystal-rich magmas that entrained residual phases (Patiño Douce 1999). We suggest that during generation, ascent and emplacement of the main unit, crustal components could have been supplied from different processes/sources: (1) initial melting of older low-crustal rocks; (2) feeding from syntectonic partially molten high-grade rocks (i.e., migmatites at middle crustal levels) and subsequent hybridization, including mixing with leucocratic pure crustal melts; and (3) assimilation of wall rock xenoliths at different crustal levels (see discussion below). Moreover, mafic components involved basic melts from the lower crust/lithospheric mantle and/or mixing with I-type magmas, as has been consistently argued for most of the Famatinian granitoids (e.g., Pankhurst et al. 2000; Grosse et al. 2011; Dahlquist et al. 2013). The lack of mafic enclaves and/or basic dykes in the LCP rejects interaction with mafic material at higher crustal levels. Conversely, leucocratic granitoids were derived exclusively from metasedimentary sources by local anatexis of the migmatitic basement underlying the emplacement level.

Constraints on emplacement conditions and timing

According to the classic conceptual model of Buddington (1959), the styles of pluton emplacement, associated

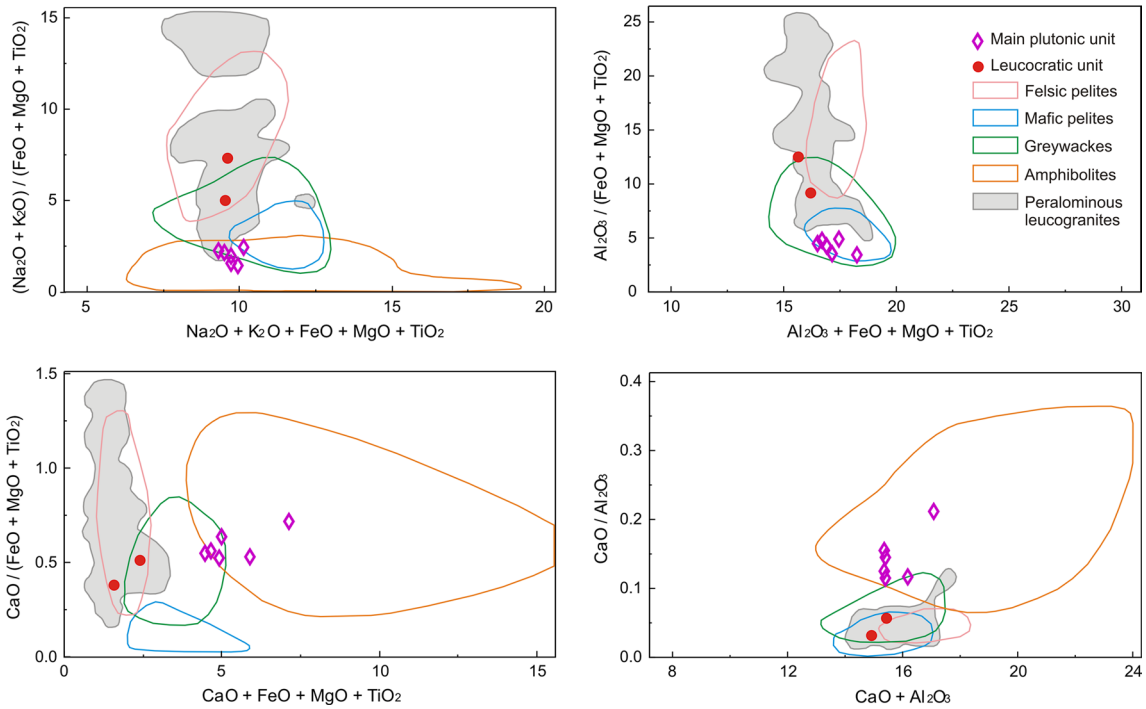

Fig. 14 Studied granitoids plotted on major element diagrams of Patiño Douce (1999). Fields are compositions of melts produced by experimental dehydration-melting, except the field of peraluminous leucogranites that correspond to natural granites of Patiño Douce (1999)

metamorphism and fabric development in intrusions may vary substantially with depth (Miller et al. 2009). Therefore, based on field relationships between metamorphic rocks from the northern part of the Sierra de Humaya and barometric calculations on migmatites of the El Portezuelo metamorphic–igneous complex from nearby areas, a rough estimation of the emplacement level for the LCP is deduced. Because the LCP is intruded into two-mica schists, no direct barometric estimations are possible (pluton and host rock) due to the lack of suitable mineral assemblages. However, structural continuity of the metamorphic foliation from two-mica schists into cordierite–garnet–K-feldspar–sillimanite migmatites in the Sierra de Humaya crustal block allows us to estimate depth levels. The highest calculated regional pressures of ~5 kbar in migmatites of the Sierra de Graciana and Sierra de Potrerillo (Larrovere et al. 2011) are consistent with metamorphism at about ~19 km depth (taking into account an average density of 2,700–2,800 kg/m^3, 1 kbar = 3.80–3.85 km). Assuming this depth level for migmatites of the Sierra de Humaya, lower pressures (depth) would correspond for the two-mica schist levels. Supposing similar vertical pressure gradients (perpendicular to the strike as maximum pressure values), the measured crustal width between two points with parallel metamorphic foliation in migmatites and schists is 4.5 km (Fig. 1). This means the current exposure of the LCP represents a maximum emplacement depth of ~14.5 km (~3.8 kbar). Regarding average continental crust thickness and divisions (0–12 km upper crust, 12–23 km middle crust, 23–40 km lower crust; Rudnick and Gao 2003), the maximum estimated emplacement depth is consistent with the upper part of the middle crust.

Brittle and ductile deformation mechanisms in the wall rock were active during pluton emplacement at this depth, as evidenced by the following field observations: (1) irregular branch-like discordant granitic dykes filling fractures, linked to meter-scale local folds in the wall rock; (2) apparent boudins of leucocratic dykes and associated wall rock deflections; (3) both angular and sheet-like compositionally identical wall rock xenoliths; (4) wall rock foliation roughly draped around the pluton but also locally truncated by the intrusion; (5) major wall rock folds; and (6) the sheeted nature of the contacts. As an alternative to brittle fracturing, ductile fracturing has been proposed as a mechanism for ductile environments (Weinberg and Regenauer-Lieb 2010), supporting the possibility of concomitant fracturing and ductile deformation at this emplacement level.

The calculated crystallization age for the LCP indicates contemporaneous magmatism, metamorphism and deformation at the orogen scale. The newly obtained age of 474.1 ± 4.3 Ma is consistent with Ordovician ages (477–470 Ma) of the high-grade metamorphic rocks of the El Portezuelo metamorphic–igneous complex (Larrovere et al. 2011). At the pluton scale, field and structural data which

support emplacement and related host rock folding include the parallel to subparallel trends in the strike of the wall rock foliation, the fold axial traces, the host rock-pluton contacts, and the long dimension of the intrusion. At the outcrop scale, evidence such as folded concordant leucocratic sheets with magmatic fabrics support the idea of syn-folding magmatism for the LCP. Localization of late magmatic intrusions (i.e., leucocratic sheets) and xenoliths on the eastern and western pluton-host rock contact suggests that these sectors are the lateral wall zones of the LCP. Intrusions associated with structures formed in the aureole (i.e., folded sheets) suggest that ductile deformation in the aureole formed prior to final solidification of the chamber (e.g., Paterson and Farris 2008).

Emplacement mechanisms

Although fabrics within plutons provide important information about emplacement in field-based structural studies, it is believed that the main clues for MTPs come from examining the host rock around the plutons, i.e., the structural aureoles (Buddington 1959; Paterson and Fowler 1993). Because the S_2 metamorphic foliation is a structure that slightly predates the emplacement of the LCP, several documented changes in the attitude of host rock markers around the LCP (but not recorded from regional orientations) indicate a strong relationship between host rock ductile deformation and pluton emplacement. Examples include (1) local folding of the host rock layering, (2) draping of the S_2 foliation around the pluton and (3) minor strike deflection of S_2 (NNW–SSE in LCP structural domain and N–S in regional domain). The most obvious evidence of the emplacement of the LCP is the ductile deformation observed in the structural aureole, i.e., rim folds. Viable emplacement mechanisms that link host rock folding with magma intrusion are (1) regional folding (e.g., Miller et al. 2009); (2) return flow (e.g., Paterson et al. 1991; He et al. 2009); (3) gravitationally driven roof/wall rotation and collapse (e.g., Paterson and Farris 2008); and (4) lateral shortening (e.g., Paterson et al. 1991; Marko and Yoshinobu 2011). Material transfer process like regional folding is inconsistent with the lack of appreciable folding in the regional domain. Because growth of folds is slow compared to magma transport rates (e.g., Paterson and Tobisch 1992) the genetic link between regional folding and emplacement has been related to the effects of the stress field (Miller et al. 2009). The regional principal shortening direction linked to an E–W compressive regime during the Famatinian orogeny (e.g., Willner et al. 1987; Le Core and Rosello 1994) in Las Chacritas zone could support this assumption; however, host rock ductile deformation concentrated exclusively in the LCP structural domain implies that magma forces played an active role in driving lateral wall rock displacements. Also, assuming that dips of contacts do not change when projecting upward, we observed in the cross section B–B′ (Fig. 2c) that the pluton largely cuts folds because the width of the pluton is larger than wavelength of folds. On the other hand, the lack of asymmetrical tight folds, steeply plunging lineations and monoclinal fabrics in wall rocks, rule out return flow (e.g., He et al. 2009), at least at the current exposure level. Predominance of outward-facing stratigraphy and rim synclines/anticlines attached to walls instead of inward-facing stratigraphy and monoclines/anticlines relationships, respectively (e.g., Paterson and Farris 2008), preclude gravitationally driven roof/wall collapse. Lastly, the lateral and upward deflections of the beds, synclines/anticlines associations, major and minor folds with subhorizontal fold axes trending parallel to the general pluton-host rock contact, and subvertical fold axial planes in the structural aureole indicate that host rocks were displaced laterally with respect to the pluton. We suggest these structural features are consistent with a lateral shortening mechanism as a result of magma emplacement (Fig. 15). This lateral shortening also implies vertical movement of host rock associated with fold formation. Lateral transport around rising/expanding magma chambers requires compensating vertical transport, and ductile downward host rock transport relative to pluton roofs is a common process during the rise of magma (Paterson and Farris 2008). Therefore, at levels below the present exposure, downward ductile flow along pluton walls could have compensated the vertical host rock displacements during emplacement of the LCP.

Because it has been widely argued that magma emplacement in the crust involves multiple MTPs (Buddington 1959; Paterson and Fowler 1993; Paterson et al. 1996; Miller et al. 2009), even for a single pluton, we cannot exclude that additional emplacement mechanisms may have contributed to create sufficient room for the emplacement of the LCP. In order to evaluate the amount of displaced host rock material by lateral shortening, longitudinal strain has been estimated for the central contact aureole (cross section B–B′; Fig. 2c) following the methodology used by Marko and Yoshinobu (2011). Although for the structural restoration some assumptions are done regarding continuity of beds at depth, fold geometry, downward pluton shape, pre-emplacement stratigraphy and strain (it assumes plane strain in the cross-sectional area and does not account for heterogeneous strain and/or volume loss in the cross-sectional plane), estimations given below (minimum values) are an acceptable approximation for the intended purpose. The extension (e) values in the cross section B–B′ are −0.43 (43 %) on the east side and −0.22 (22 %) on the west side. Thus, total shortening by folding in the structural aureole is 65 %. This total aureole shortening accommodates ~40 % of the width of the pluton in the

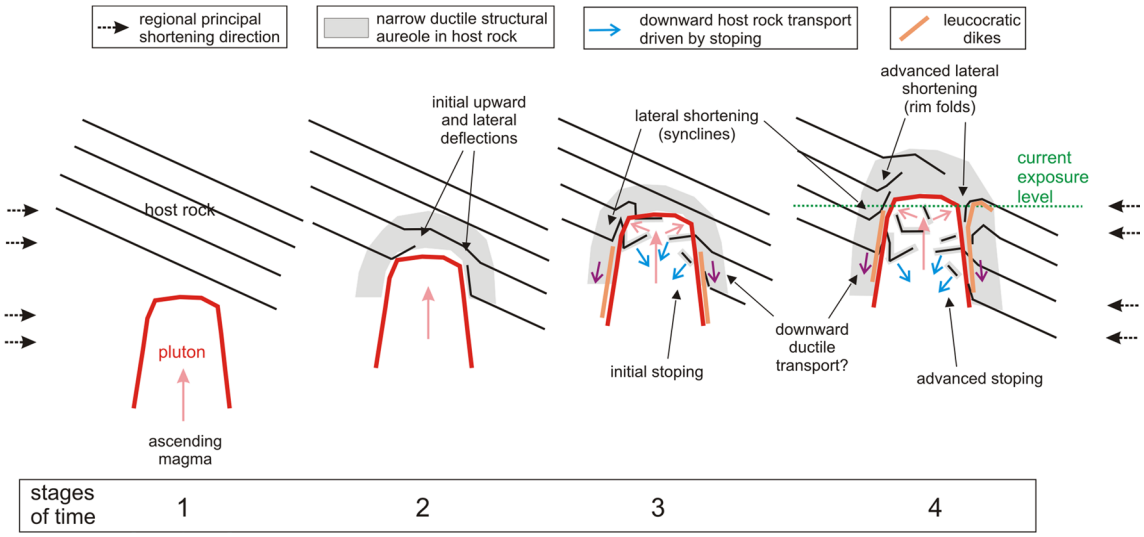

Fig. 15 Schematic emplacement model for the LCP. Pluton shape is also schematic. Stages 1 and 2: ascent and early pluton emplacement dominated by initial upward and lateral host rock deflections. Pluton intrudes the host rocks cutting in high angle the preexisting metamorphic foliation generating an incipient structural aureole. Stage 3: increasing host rock displacement by lateral shortening and initial downward host rock transport driven by stoping. Stage 4: late pluton emplacement dominated by multiple material transfer processes, i.e., advanced lateral shortening and stoping. The structural aureole is represented by dominant rim folds

central part, evidencing that additional MTPs are necessary to generate the remaining amount of room for the emplacement of the pluton.

Preserved wall rock xenoliths in the contact zone, partial local truncations of the host rock metamorphic foliation and fold traces, and inferred cutting relationships between pluton and folds from upward pluton projections are consistent with magmatic stoping. Because aureole ductile strains are insufficient (~40 %) to accommodate the magma emplaced, we suggest that stoping could be a complementary mechanism to create the necessary space for the emplacement of the LCP (Fig. 15). Most of the missing host rock material from the space now occupied by part of the pluton must have been transported downward to levels below the present exposure, as it has been postulated by several studies (e.g., Yoshinobu et al. 2003; Paterson and Farris 2008; Miller et al. 2009). Further, whole-rock geochemistry support assimilation of crustal material during magma evolution. Processes of disaggregation and mixing of metasedimentary stoped blocks have been demonstrated in previous works (e.g., Clarke et al. 1998). Although P–T conditions at the structural level where the LCP was emplaced are compatible with dominant ductile deformation mechanisms, it has been recognized that magmatic stoping, which has historically been considered a shallow-level mechanism, may occur at all crustal levels (Miller et al. 2009). This assumption agrees with the observed structures described above that support concomitant fracturing and ductile deformation at this emplacement level. Even if field observations suggest that stoping was a relatively late process with respect to aureole ductile deformation, we cannot rule out the idea that stoping have operated from early stages of the magma intrusion.

Conclusions

From the physicochemical behavior of a magmatic body in the Sierra de Humaya, NW Argentina, named the LCP at a mid-crustal level, we derive the following conclusions:

1. LCP is a composite pluton formed by peraluminous two-mica granitoids and minor muscovite ± tourmaline ± garnet leucocratic granitoids. The former are hybrid granitoids generated by interaction of crustal rocks with mafic magmas and/or crystal-rich magmas that entrained residual phases, whereas the leucocratic granitoids are pure crustal melts originated by anatexis of metasedimentary rocks.
2. The pluton was emplaced in the upper middle crust at a depth of ~14.5 km, where major host rock structures synchronous with emplacement are ductile. However, concomitant fracturing was active during pluton emplacement at this depth.
3. The emplacement of the LCP was coeval with regional Ordovician Famatinian metamorphism, with a magmatic crystallization age of 474.1 ± 4.3 Ma. Syn-folding magmatism is supported by structural features at outcrop and pluton scale such as folded concordant leucocratic sheets with magmatic fabrics.

4. Several changes in the attitude of host rock markers around the LCP, not recorded by regional orientations, indicate a strong relationship between host rock ductile deformation and pluton emplacement. Therefore, aureole rim folds and strike deflections of host rocks occurred as a result of magma intrusion.
5. Aureole shortening by folding accommodated ~40 % of the width of the pluton, indicating that additional MTPs were necessary to generate the remaining amount of room for growth of the pluton.
6. For the emplacement of the LCP, we infer a concomitant interplay between lateral shortening and magmatic stoping as the dominant processes for magma chamber construction. However, we cannot exclude that additional MTPs may have contributed to the emplacement of the LCP, especially at different crustal levels not currently exposed.
7. Magmatic stoping supports, at least partially, the crustal geochemical character of the LCP, and evidence that the origin and evolution of plutons involve complex physicochemical interactions.
8. The example presented in this paper shows that multiple MTPs are a common feature in the emplacement of plutons, as has lately been proposed by other authors.

Acknowledgments We thank T. Theye for introduction to microprobe and monazite dating and H-J Massonne for using the laboratories at Institut für Mineralogie und Kristallchemie (Stuttgart). We acknowledge J. de la Rosa (UHU) for providing some whole-rock chemical analysis. We thank C. Bustamante (CRILAR-CONICET) for technical support and S. Hartman (USC) for English edition. We also thank S.R. Paterson (USC) for commenting on earlier versions of the manuscript. We are grateful to S. Luna and all the staff of the rural School N° 422 of the Las Chacritas town for hospitality and lodging during field work. We thank J. Palavecino for his help with field work. We thank also J.M. Tubía and J. Žák for constructive reviews, and M.A. Elburg for his editorial handling. C. de los Hoyos acknowledges support from a postdoctoral fellowship from the DAAD. This work was supported through funding from SECyT-UNLaR to P. Alasino and M. Larrovere.

References

Aceñolaza FG, Toselli AJ (1973) Consideraciones estratigráficas y tectónicas sobre el paleozoico inferior del noroeste argentino. 2° Congr Latinoam Geol Caracas, pp 755–763

Adams CJ, Miller H, Aceñolaza FG, Toselli AJ, Griffin WL (2011) The Pacific Gondwana margin in the late Neoproterozoic–early Paleozoic: detrital zircon U–Pb ages from metasediments in northwest Argentina reveal their maximum age, provenance and tectonic setting. Gondwana Res 19:71–83. doi:10.1016/j.gr.2010.05.002

Baldo E, Casquet C, Rapela CW, Pankhurst RJ, Galindo C, Fanning C, Saavedra J (2001) Ordovician metamorphism at the southwestern margin of Gondwana: P-T conditions and U–Pb SHRIMP ages from Loma de Las Chacras, Sierras Pampeanas. III Simp Sudam Geol Isotópica, pp 544–547

Beard JS, Lofgren GE (1991) Dehydration melting and water-satured melting of basaltic and andesitic greenstones and amphibolites at 1, 3, and 6.9 kbar. J Pet 32:365–401

Bons PD, Druguet E, Hamann I, Carreras J, Passchier CW (2004) Apparent boudinage in dykes. J Struct Geol 26:625–636. doi:10.1016/j.jsg.2003.11.009

Brown M, Solar GS (1998a) Shear-zone systems and melts: feedback relations and self-organization in orogenic belts. J Struct Geol 20:211–227

Brown M, Solar GS (1998b) Granite ascent and emplacement during contractional deformation in convergent orogens. J Struct Geol 20:1365–1393. doi:10.1016/S0191-8141(98)00074-1

Buddington AF (1959) Granite emplacement with special reference to North America. Geol Soc Am Bull 70:671–747

Büttner SH, Glodny J, Lucassen F, Wemmer K, Erdmann S, Handler R, Franz G (2005) Ordovician metamorphism and plutonism in the Sierra de Quilmes metamorphic complex: implications for the tectonic setting of the northern Sierras Pampeanas (NW Argentina). Lithos 83:143–181. doi:10.1016/j.lithos.2005.01.006

Casquet C, Rapela CW, Pankhurst RJ, Baldo E, Galindo C, Fanning CM, Dahlquist J (2012) Fast sediment underplating and essentially coeval juvenile magmatism in the Ordovician margin of Gondwana, Western Sierras Pampeanas, Argentina. Gondwana Res 22:664–673. doi:10.1016/j.gr.2012.05.001

Chernicoff CJ, Zappettini EO, Santos JOS, Allchurch S, McNaughton NJ (2010) The southern segment of the Famatinian magmatic arc, La Pampa Province, Argentina. Gondwana Res 17:662–675. doi:10.1016/j.gr.2009.10.008

Chew D, Schaltegger U, Kosler J, Whitehouse M, Gutjahr M, Spikings R, Miskovic A (2007) U–Pb geochronologic evidence for the evolution of the Gondwanan margin of the north-central Andes. GSA Bull 119:697–711

Cisterna CE (2003) Faja Intrusiva La Majada, sierra de Ancasti, Catamarca: caracterización petrológica-estructural. Rev la Asoc Geológica Argentina 58:20–30

Cisterna CE, Medina ME, Fernández Turiel L (2004) Evidencias de procesos de fraccionamiento y mezcla de magmas en el Complejo Intrusivo Las Angosturas, Sistema de Famatina. Rev la Asoc Geológica Argentina 59:45–56

Clarke DB, Henry AS, White MA (1998) Exploding xenoliths and the absence of "elephants" graveyards' in granite batholiths. J Struct Geol 20:1325–1343. doi:10.1016/S0191-8141(98)00082-0

Conrad WK, Nicholls IA, Wall VJ (1988) Water-satured and undersatured melting of metaluminous and peraluminous crustal composition at 10 kb: evidence for the origin of silicic magmas in the Taupo Volcanic Zone, New Zealand, and other ocurrences. J Pet 29:765–803

Dahlquist JA, Galindo C (2004) Geoquímica isotópica de los granitoides de la sierra de Chepes: un modelo geotectónico y termal, implicancias para el orógeno famatiniano. Rev la Asoc Geológica Argentina 59:57–69

Dahlquist JA, Rapela CW, Baldo EG (2005) Petrogenesis of cordierite-bearing S-type granitoids in Sierra de Chepes, Famatinian orogen, Argentina. J S Am Earth Sci 20:231–251. doi:10.1016/j.jsames.2005.05.014

Dahlquist JA, Galindo C, Pankhurst RJ, Rapela CW, Alasino PH, Saavedra J, Fanning CM (2007) Magmatic evolution of the Peñón Rosado granite: petrogenesis of garnet-bearing granitoids. Lithos 95:177–207. doi:10.1016/j.lithos.2006.07.010

Dahlquist JA, Pankhurst RJ, Rapela CW, Galindo C, Alasino P, Fanning CM, Saavedra J, Baldo EG (2008) New SHRIMP U–Pb data from the Famatina complex: constraining early-mid Ordovician Famatinian magmatism in the Sierras Pampeanas, Argentina. Geol Acta 6:319–333

Dahlquist JA, Rapela CW, Pankhurst RJ, Fanning CM, Vervoort JD, Hart G, Baldo EG, Murra JA, Alasino PH, Colombo F (2012)

Age and magmatic evolution of the Famatinian granitic rocks of Sierra de Ancasti, Sierras Pampeanas, NW Argentina. J S Am Earth Sci 34:10–25. doi:10.1016/j.jsames.2011.07.006

Dahlquist JA, Pankhurst RJ, Gaschnig RM, Rapela CW, Casquet C, Alasino PH, Galindo C, Baldo EG (2013) Hf and Nd isotopes in Early Ordovician to Early Carboniferous granites as monitors of crustal growth in the Proto-Andean margin of Gondwana. Gondwana Res 23:1617–1630. doi:10.1016/j.gr.2012.08.013

De la Rosa JD, Chacón H, Sánchez de la Campa A, Carrasco R, Nieto JM (2001) Metodología y análisis de elementos trazas-REE mediante ICP-MS del Standart SARM 1 granito y SARM 4 norita. 3° Congr Ibérico Geoquímica Zaragoza, pp 435–438

De los Hoyos CR, Willner AP, Larrovere MA, Rossi JN, Toselli AJ, Basei MAS (2011) Tectonothermal evolution and exhumation history of the Paleozoic Proto-Andean Gondwana margin crust: the Famatinian Belt in NW Argentina. Gondwana Res 20:309–324. doi:10.1016/j.gr.2010.12.004

Debon F, Le Fort P (1983) A chemical–mineralogical classification of common plutonic rocks and associations. Trans R Soc Edinb Earth Sci 73:135–149

Ducea MN, Otamendi JE, Bergantz G, Stair KM, Valencia VA, Gehrels GE (2010) Timing constraints on building an intermediate plutonic arc crustal section: U–Pb zircon geochronology of the Sierra Valle Fértil–La Huerta, Tectonics. Famatinian arc, Argentina. doi:10.1029/2009TC002615

Escayola MP, van Staal CR, Davis WJ (2011) The age and tectonic setting of the Puncoviscana Formation in northwestern Argentina: an accretionary complex related to early Cambrian closure of the Puncoviscana Ocean and accretion of the Arequipa-Antofalla block. J S Am Earth Sci 32:438–459. doi:10.1016/j.jsames.2011.04.013

Fernández C, Becchio R, Castro A, Viramonte JM, Moreno-Ventas I, Corretgé LG (2008) Massive generation of atypical ferrosilicic magmas along the Gondwana active margin: implications for cold plumes and back-arc magma generation. Gondwana Res 14:451–473. doi:10.1016/j.gr.2008.04.001

Frost BR, Barnes CG, Collins WJ, Arculus RJ, Ellis DJ, Frost CD (2001) A geochemical classification for granitic rocks. J Pet 42:2033–2048

González Bonorino F (1950) Descripción geológica de la Hoja 13e, Villa Alberdi (Catamarca–Tucumán). Dirección Nacional de Minería. Boletín 74, p 78, Buenos Aires. 78

Grosse P, Bellos LI, de los Hoyos CR, Larrovere MA, Rossi JN, Toselli AJ (2011) Across-arc variation of the Famatinian magmatic arc (NW Argentina) exemplified by I-, S- and transitional I/S-type Early Ordovician granitoids of the Sierra de Velasco. J S Am Earth Sci 32:110–126. doi:10.1016/j.jsames.2011.03.014

He B, Xu Y-G, Paterson S (2009) Magmatic diapirism of the Fangshan pluton, southwest of Beijing, China. J Struct Geol 31:615–626. doi:10.1016/j.jsg.2009.04.007

Hickey RL, Frey FA, Gerlach DC, López-Escobar L (1986) Multiple sources for basaltic arc rocks from the southern volcanic zone of the andes (34°–41°S): trace element and isotopic evidence for contributions from subducted oceanic crust, mantle, and continental crust. J Geophys Res 91:5963–5983

Hogan J, Price J, Gilbert M (1998) Magma traps and driving pressure: consequences for pluton shape and emplacement in an extensional regime. J Struct Geol 20:1155–1168

Hongn FD, Tubía JM, Esteban JJ, Aranguren A, Vegas N, Sergeev S, Larionov A, Basei M (2014) The Sierra de Cachi (Salta, NW Argentina): geological evidence about a Famatinian retro-arc at mid crustal levels. J Iber Geol 40:225–240. doi:10.5209/rev_JIGE.2014.v40.n2.45303

Jordan T, Allmendinger R (1986) The Sierras Pampeanas of Argentina: a modern analogue of rocky mountain foreland deformation. Am J Sci 286:737–764

Knüver M (1983) Dataciones radimétricas de rocas plutónicas y metamórficas. In: Aceñolaza FG, Miller H, Tosellil A (eds) La Geología de la Sierra de Ancasti. Münstersche Forschungen zur Geologie und Paläontologie, vol 59. Words in German, Münster, pp 201–218

Larrovere MA (2009) Petrología de la faja migmatítica entre el flanco noroccidental de la Sierra de Ancasti, su continuación en la Sierra de Aconquija y el flanco nororiental de la Sierra de Ambato. Doctoral thesis, Universidad Nacional de Córdoba (unpublished), p 234

Larrovere MA, de los Hoyos CR, Toselli AJ, Rossi JN, Basei MAS, Belmar ME (2011) High T/P evolution and metamorphic ages of the migmatitic basement of northern Sierras Pampeanas, Argentina: characterization of a mid-crustal segment of the Famatinian belt. J S Am Earth Sci 31:279–297. doi:10.1016/j.jsames.2010.11.006

Larrovere MA, de los Hoyos CR, Grosse P (2012) Los complejos metamórficos del retro-arco Famatiniano (noroeste de Argentina): caracterización geoquímica e isotópica de sus protolitos e implicancias geotectónicas. Rev Mex Ciencias Geológicas 29:676–695

Le Core CA, Rosello EA (1994) Kinematics of early Paleozoic ductile deformation in the basement of NW Argentina. J S Am Earth Sci 7:301–308

Llambías EJ, Sato AM, Suarez AO, Prozzi C (1998) The granitoids of the Sierra de San Luis. Geol Soc Lond Spec Publ 142:325–341. doi:10.1144/GSL.SP.1998.142.01.16

López de Luchi MG, Siegesmund S, Wemmer K, Steenken A, Naumann R (2007) Geochemical constraints on the petrogenesis of the Paleozoic granitoids of the Sierra de San Luis, Sierras Pampeanas, Argentina. J S Am Earth Sci 24:138–166. doi:10.1016/j.jsames.2007.05.001

Lucassen F, Becchio R (2003) Timing of high-grade metamorphism: early Palaeozoic U–Pb formation ages of titanite indicate long-standing high-T conditions at the western margin of Gondwana (Argentina, 26–29°S). J Metamorph Geol 21:649–662. doi:10.1046/j.1525-1314.2003.00471.x

Lucassen F, Franz G (2005) The early Palaeozoic Orogen in the Central Andes: a non-collisional orogen comparable to the Cenozoic high plateau? Geol Soc Lond Spec Publ 246:257–273. doi:10.1144/GSL.SP.2005.246.01.09

Marko WT, Yoshinobu AS (2011) Using restored cross sections to evaluate magma emplacement, White Horse Mountains, Eastern Nevada, USA. Tectonophysics 500:98–111. doi:10.1016/j.tecto.2010.05.001

Miller CF, Stoddard EF, Bradfish LJ, Dollase WA (1981) Composition of plutonic muscovite: genetic implications. Can Mineral 19:25–34

Miller RB, Paterson SR, Matzel JP (2009) Plutonism at different crustal levels: insights from the ~5–40 km (paleodepth) North Cascades crustal section, Washington. In: Miller RB, Snoke AW (eds) Crustal Cross Sect. from West. North Am. Cordillera Elsewhere Implic Tecton Petrol Process. Geological Society of America, Special Papers, vol 456, pp 1–26

Montel J, Foret S, Veschambre M, Nicollet C, Provost A (1996) Electron microprobe dating of monazite. Chem Geol 131:37–53

Montel JM, Kornprobst J, Vielzeuf D (2000) Preservation of old U–Th–Pb ages in shielded monazite; example from the Benmi Bousera Hercynian kinzigites (Morocco). J Metamorph Geol 18:335–342

Morosini A, Ortiz A, Ramos G (2009) Los granitoides famatinianos del sector suroccidental de la Sierra de San Luis: clasificación y geotermometría. Rev la Asoc Geológica Argentina 64:433–446

Murray RW, Miller DJ, Kryc KA (2000) Analysis of mayor and trace elements in rocks, sediments, and interstitial waters by inductively coupled plasma–atomic emission spectrometry (ICP–AES). ODP Tech. Note, 29 (Online). http://www-odp.tamu.edu/publications/tnotes/tn29/INDEX.HTM

Nabelek PI, Glascock MD (1995) REE-depleted leucogranites, Black Hills, South Dakota: a consequence of disequilibrium melting of monazite-bearing schists. J Pet 36:1055–1071

Nakamura N (1974) Determination of REE, Ba, Fe, Mg, Na and K in cabonaceous and ordinary chondrites. Geochim Cosmochim Acta 38:757–775

Otamendi JE, Tibaldi AM, Vujovich GI, Viñao GA (2008) Metamorphic evolution of migmatites from the deep Famatinian arc crust exposed in Sierras Valle Fértil–La Huerta, San Juan, Argentina. J S Am Earth Sci 25:313–335. doi:10.1016/j.jsames.2007.09.001

Otamendi JE, Ducea MN, Tibaldi AM, Bergantz GW, de la Rosa JD, Vujovich GI (2009) Generation of tonalitic and dioritic magmas by coupled partial melting of gabbroic and metasedimentary rocks within the deep crust of the Famatinian magmatic arc, Argentina. J Pet 50:841–873. doi:10.1093/petrology/egp022

Otamendi JE, Cristofolini E, Tibaldi AM, Quevedo FI, Baliani I (2010) Petrology of mafic and ultramafic layered rocks from the Jaboncillo Valley, Sierra de Valle Fértil, Argentina: implications for the evolution of magmas in the lower crust of the Famatinian arc. J S Am Earth Sci 29:685–704. doi:10.1016/j.jsames.2009.11.001

Otamendi JE, Ducea MN, Bergantz GW (2012) Geological, petrological and geochemical evidence for progressive construction of an arc crustal section, Sierra de Valle Fertil, Famatinian Arc, Argentina. J Pet 53:761–800. doi:10.1093/petrology/egr079

Pankhurst RJ, Rapela CW, Saavedra J, Baldo E, Dahlquist J, Pascua I, Fanning CM (1998) The Famatinian magmatic arc in the central Sierras Pampeanas: an Early to Mid-Ordovician continental arc on the Gondwana margin. Geol Soc Lond Spec Publ 142:343–367. doi:10.1144/GSL.SP.1998.142.01.17

Pankhurst RJ, Rapela CW, Fanning CM (2000) Age and origin of coeval TTG, I- and S-type granites in the Famatinian belt of NW Argentina. Trans R Soc Edinb Earth Sci 91:151–168

Paterson SR, Farris DW (2008) Downward host rock transport and the formation of rim monoclines during the emplacement of Cordilleran batholiths. Trans R Soc Edinb Earth Sci 97:397–413

Paterson SR, Fowler TK (1993) Re-examining pluton emplacement processes. J Struct Geol 115:191–206

Paterson SR, Tobisch OT (1992) Rates of processes in arcs: implications for timing and nature of pluton emplacement and wall rock deformation. J Struct Geol 14:291–300

Paterson SR, Vernon RH, Fowler TK (1991) Aureole Tectonics. In: Kerrick DM (ed) Contact Metamorph. Rev. in Mineralogy, Mineral Soc Amer, vol 26, pp 105–206

Paterson SR, Fowler TK, Miller RB (1996) Pluton emplacement in arcs: a crustal-scale exchange process. In: Brown M, Candela PA, Peck DL et al (eds) The third hutton simposium on the origin of granites and related rocks, vol 315. Geological Society of America, Special Papers, Maryland, pp 115–123

Patiño Douce AE (1999) What do experiments tell us about the relative contributions of crust and mantle to the origin of granitic magmas? In: Castro A, Fernández C, Vigneresse JL (eds) Understanding granites: integrating new and classical techniques. Geological Society of London, Special Publications, vol 168, pp 55–75

Pattison DRM, Tracy RJ (1991) Phase equilibria and thermobarometry of metapelites. In: Kerrick DM (ed) Contact Metamorph. Reviews in Mineralogy and Geochemistry, Mineralogical Society of America, vol 26, pp 105–206

Rapela CW, Toselli AJ, Heaman L, Saavedra J (1990) Granite plutonism of the Sierras Pampeanas: an inner cordilleran Paleozoic arc in the southern Andes. In: Kay SM, Rapela CW (eds) Plutonism from Antarct. to Alaska. Geological Society of America, Special Papers, vol 241, pp 77–90

Reed SJB, Buckley A (1998) Rare-earth element determination in minerals by electron-probe micro-analysis: application of spectrum synthesis. Mineral Mag 62:1–8

Reissinger M (1983) Evolución geoquímica de las rocas plutónicas. In: Aceñolaza FG, Miller H, Toselli A (eds) La Geol. La Sierra Ancasti. Münstersche Forschungen zur Geologie und Paläontologie, vol 59, pp 101–112

Rossi JN, Toselli AJ, Saavedra J, Sial AN, Pellitero E, Ferreira VP (2002) Common crustal source for contrasting peraluminous facies in the early paleozoic capillitas Batholith, NW Argentina. Gondwana Res 5:325–337

Rudnick RL, Gao S (2003) Composition of the continental crust. In: Rudnick RL (ed) Crust treatise on geochemistry, vol 3. Elsevier, Amsterdam, pp 1–64

Saavedra J, Toselli A, Rossi J, Pellitero E, Durand F (1998) The early Palaeozoic magmatic record of the Famatina system: a review. Geol Soc Lond Spec Publ 142:283–295. doi:10.1144/GSL.SP.1998.142.01.14

Sato AM, González PD, Llambías EJ (2003) Evolución del orógeno Famatiniano en la Sierra de San Luis: magmatismo de arco, deformación y metamorfismo de bajo a alto grado. Rev la Asoc Geológica Argentina 58:487–504

Scherrer NC, Engi M, Gnos E, Jakob V, Liechti A (2000) Monazite analysis; from sample preparation to microprobe age dating and REE quantification. Schweizerische Mineral und Petrogr Mitteilungen 80:93–105

Sola AM, Becchio RA (2010) Leucogranito Pumayaco: anatexis cortical durante el Ciclo Orogénico Famatiniano en el extremo norte de la Sierra de Molinos, provincia de Salta. Rev la Asoc Geológica Argentina 66:206–224

Solar GS, Brown M (2001) Petrogenesis of Migmatites in Maine, USA: possible Source of Peraluminous Leucogranite in Plutons? J Pet 42:789–823

Speer JA (1984) Micas in igneous rocks. Rev Mineral Geochem 13:299–356

Steenken A, López de Luchi MG, Martínez Dopico C, Drobe M, Wemmer K, Siegesmund S (2011) The Neoproterozoic-early Paleozoic metamorphic and magmatic evolution of the Eastern Sierras Pampeanas: an overview. Int J Earth Sci 100:465–488. doi:10.1007/s00531-010-0624-0

Toselli AJ (1992) El magmatismo del noroeste argentino. Universida, Reseña sistemática e interpretación 243

Toselli A, Reissinger M, Durand FR, Bazán C (1983) Rocas graníticas. In: Aceñolaza FG, Miller H, Toselli A (eds) La Geol. La Sierra Ancasti. Münstersche Forschungen zur Geologie und Paläontologie, vol 59, pp 79–99

Toselli AJ, Sial AN, Saavedra J, Rossi de Toselli JN, Pinto Ferreira V (1996) Geochemistry and genesis of the S-type, cordierite-andalusite-bearing capillitas Batholith, Argentina. Int Geol Rev 38:1040–1053

Vielzeuf D, Holloway JR (1988) Experimental determination of the fluid-absent melting relations in the pelitic system. Consequences for crustal differentiation. Contrib Mineral Pet 98:257–276

Villaseca C, Barbero L, Herreros V (1998) A re-examination of the typology of peraluminous granite types in intracontinental orogenic belts. Trans R Soc Edinb Earth Sci 91:151–168

Vujovich GI (1994) Geología del basamento ígneo-metamórfico de la loma de Las Chacras, sierra de La Huerta, San Juan. Rev la Asoc Geológica Argentina 49:321–336

Weinberg RF, Regenauer-Lieb K (2010) Ductile fractures and magma migration from source. Geology 38:363–366. doi:10.1130/G30482.1

Weinberg RF, Sial AN, Mariano G (2004) Close spatial relationship between plutons and shear zones. Geology 32:377. doi:10.1130/G20290.1

Williams ML, Jercinovic MJ, Goncalves P, Mahan K (2006) Format and philosophy for collecting, compiling, and reporting microprobe monazite ages. Chem Geol 225:1–15. doi:10.1016/j.chemgeo.2005.07.024

Williams ML, Jercinovic MJ, Hetherington CJ (2007) Microprobe Monazite geochronology: understanding geologic processes by integrating composition and chronology. Annu Rev Earth Planet Sci 35:137–175. doi:10.1146/annurev.earth.35.031306.140228

Willner AP, Lottner US, Miller H (1987) Early Paleozoic structural development in the NW Argentine basement of the Andes and its implication for geodynamic reconstructions. In: McKenzie GD (ed) Gondwana 6 Struct. Tectonics Geophys. American Geophysical Union Monograph, New York, pp 229–239

Willner AP, Miller H, Jezek P (1990) Composición geoquímica del basamento sedimentario-metamórfico de los Andes del NW Argentino (Precámbrico superior-Cámbrico inferior). In: Aceñolaza FG, Miller H, Toselli AJ (eds) El Ciclo Pampeano en el noroeste Argentino. Universidad Nacional de Tucumán, Serie Correlación Geológica, vol 4, pp 161–179

Yoshinobu AS, Fowler TK, Paterson SR, Llambias E, Tickyj H, Sato AM (2003) A view from the roof: magmatic stoping in the shallow crust, Chita pluton, Argentina. J Struct Geol 25:1037–1048